International Journal of Mechanical Sciences 242 (2023) 108023

Contents lists available at ScienceDirect

International Journal of Mechanical Sciences

journal homepage: www.elsevier.com/locate/ijmecsci

Application of magnetic field to reduce the forced response of steel bridges to high speed train

Mustafa Eroğlu [a,*], Mehmet Akif Koç [b], İsmail Esen [c]

[a] Engineering Faculty, Mechanical Engineering Department, Sakarya University, Sakarya 54187, Turkey
[b] Technology Faculty, Mechatronics Engineering Department, Sakarya Applied Sciences University, Sakarya 54187, Turkey
[c] Engineering Faculty, Mechanical Engineering Department, Karabük University, Karabük 78050, Turkey

ARTICLE INFO

Keywords:
Train-track-bridge interaction
Magnetic field
Euler-Bernoulli beam
Simulation program
Runge-Kutta method

ABSTRACT

This paper uses a train-track-bridge interaction system to assess the dynamic performance of railway bridges exposed to a high-speed train and magnetic field. A 24° of freedom 3D train model and thin steel bridge beam are considered. In the interaction of train and bridge, a new six-parameter track system consisting of rail, sleeper, and ballast is modeled. The governing equations of the bridge, track and train motions are derived based on the Lagrange method. The Lorentz force induced by the directed magnetic field in the axial direction is obtained by Maxwell's equation. Using state-space forms, the second-order equations of motion are transformed into first-order differential equations, which are then solved using the Runge-Kutta method. Studies using parametric data are done to show how the suggested approach may be used to investigate the dynamic interaction of the entire system. The magnetic field intensities and moving train speed on the interaction of the railway bridge system were investigated and analyzed for the first time in the literature. Depending on the speed of the vehicle, when the dimensionless magnetic field is H_x^m=30, it can be seen that the train body's vertical displacement falls by around 50%. The obtained results are helpful for the design of railway bridges and the safe and comfortable ride of high-speed trains over flexible structures.

1. Introduction

Due to the ever-increasing high speeds, infrastructure systems such as railways and other bridges require sufficiently sensitive engineering work because vibration and noise at high speeds shorten the life of railway vehicles and reduce passenger comfort. In addition, trains generally reduce their speed when passing over flexible structures such as bridges to ensure driving safety. This situation causes a decrease in transportation speed and economic loss. Therefore, vibration analysis of railway bridges exposed to high-speed trains is crucial for passenger comfort and driver safety. Studies of dynamic interaction between high-speed trains and bridges date back to earlier times [1]. The modeling of the train to an analysis of the interaction system is a crucial stage. Looking at the vehicle models from the past to the present, the constant force model moves on the simply supported beam proposed by Fryba [2]. Later on, train-bridge interaction (TBi) with 2 degrees of freedom (DoFs) [3–6] and 4 DoFs [7–9] models were proposed. In addition, the quarter train model [10–12], half train model [13–17], and full train models [18–21] are also studied. TBi and TTBi with ballasted track analysis are used to determine railway dynamics. In this context, Wang et al. measured the aerodynamic forces of the high-speed train moving on the truss bridge using the TBi model [22]. Stoura and Dimitrakopoulos [23] study the extra dampening effect on bridges caused by vehicle-bridge contact. Yau et al. provide a comparable extra dampening approach for short-span railway bridges to incorporate TBi effects [24]. Zhang et al. analyzed the dynamic response of bridge and vehicle by considering variable speeds [25]. Koç et al. conducted the dynamic responses of the TBi model, taking into account the mass and speed of the train, as well as the stiffness of the rail [26]. However, for almost 200 years, railway lines have been built on ballasted tracks, and TBi studies have been insufficient [27]. Therefore, Xu et al. conducted a dynamic response analysis of long-span bridges and railway vehicles using the mode superposition method [28]. Zhai et al. introduce the framework for modeling and superposition method to model the bridge in the TTBi system [29]. To reduce the computational cost of solving the dynamic interaction in the TTBi analysis, Zhu provided the various domain frequency properties of the TTBi's dynamic responses [30]. A strategy for resolving the train-track-bridge interaction problem is presented by

* Corresponding author.
E-mail address: mustafaeroglu@sakarya.edu.tr (M. Eroğlu).

https://doi.org/10.1016/j.ijmecsci.2022.108023
Received 19 September 2022; Received in revised form 2 December 2022; Accepted 8 December 2022
Available online 9 December 2022

Melo et al. [31].

In addition, when the literature is examined, it is seen that railway bridges can generally be modeled as simply supported beams. Beam theories such as Timoshenko and Euler-Bernoulli are often preferred to model vibration analysis of beams. For example, Hirzinger et al. determined the dynamic responses of the bridge exposed to the moving mass-spring-damper system [32]. The dynamic response of a ballasted track railway bridge was studied by Tahiri et al. using a composite Euler-Bernoulli beam with two layers [33]. König et al. proved the dynamic behavior of the bridge in various configurations by modeling the bridge beams in high-speed trains in accordance with the Euler-Bernoulli theorem and taking into account the vehicle-track-bridge-soil interaction [34]. Zhen et al. discuss the steady-state responses of an infinite Euler-Bernoulli beam sitting on a nonlinear foundation while being subjected to a harmonic moving load [35].

In Timoshenko beams, the beam's rotational inertia and shear strain are considered, unlike Euler-Bernoulli beams. In this context, Esen examined the dynamic responses of the Timoshenko beam subjected to a variable velocity moving mass and an accelerating load [36,37]. Pala investigated the damped vibrations of cracked Timoshenko beams supported by springs and damping elements [38]. In some studies, the dynamic response of beams has been compared by applying both beam theories [14,39,40]. Many researchers have used methods to solve the motion equations by using the models mentioned above, such as Newmark β method [18,41–44], Wilson θ method [45,46], FEM [47–51], moving load convolution integral method (MLCIM) [11], Runge–Kutta method [26,52–54], Zhai method [55], differential quadrature method (DQM) [56–60].

Furthermore, numerous studies on Functionally Graded (FG) beams exist in the literature. For example, Gang et al. evaluated the stiffness matrix of FG nanoplate using Gaussian process regression (GPR) [61]. Using a continuous nonlocal model, Huang et al. investigate the vibrational and critical circular velocity characteristics of FG rotating microdisc [62]. Kumar et al. developed a refined trigonometric high-order shear deformation theory combined with nonlocal theory to describe the vibration response of FG porous nanoplate [63]. An exact transfer matrix method was developed in a paper to analyze the free vibration characteristics of the FG beam [64].

There are also studies on the dynamic and static behavior of beams exposed to a magnetic field or thermal effects. In this context, Jalaei et al. examined the dynamic behavior of nanobeams, which they modeled according to the Timoshenko beam theorem, in the presence of magnetic and thermal effects [65]. Arani and Jalaei examined the dynamic response of the viscoelastic graphene sheet exposed to the longitudinal magnetic field [66]. In a thermal environment, Esen et al. investigated buckling stability and free vibration analysis of microbeams modeled as Euler-Bernoulli subjected to the magnetic field [67,68]. In another study, the same author examined the dynamic behavior of Timoshenko beams modeled in micro dimensions subjected to a moving mass in a magnetic field [69]. Bai et al. studied the vibrations of hygro-thermo-magnetically based nanobeams [70]. Ebrahimi and Dabbagh investigated the effect of a magnetic field on rotary double-nanobeam systems [71]. The dynamic and instability assessments of nanobeams with viscoelastic cores under the influence of magnetic fields were clarified by Sobhy and Abazid [72].

1.1. The novelty of the present study

Different models and theories for determining the dynamic behavior of trains and bridges in the literature have been summarized above. In addition, no literature deals with how magnetic field applied to railway bridges affect train dynamics. Therefore, the primary aim of this study is to develop a simulation model of a train track bridge system with a full vehicle model by applying different magnetic field intensities to the steel bridge. Also, none of the above references have studied the analysis of the TTBi system, taking into account the railway bridges under the effect of magnetic fields. In this study, a magnetic field application that decreases the vibrations caused by the interaction of the bridge with the train has been studied so that the train's speed does not need to be reduced while passing over the bridge. The equations for the bridge, described as an Euler-Bernoulli beam, contain the transverse Lorentz force generated by the magnetic field using Maxwell's equation. As a result of this study, it is seen that the vibrations affecting the train are reduced due to the more rigid behavior of the beams in the magnetic field. In other words, to increase passenger comfort and driving safety in railway vehicles, vibrations can be reduced by managing the magnetic field effect without needing an active suspension system. Thanks to this study, one can investigate the dynamic behaviors of the bridge beam and train, considering the magnetic field and the train speed.

1.2. The organizations of the present study

The rest of this article is divided into the following sections: In Section 2, modeling of the train-track-bridge system is conducted. The equations of motion for TTBi are found using the Lagrangian approach in Section 3, which also determines the Lorentz force acting on the beams owing to the magnetic field. In Section 4, the validation of the Runge-Kutta method proposed in this study and the numerical results are given. The main conclusion is presented in Section 5.

2. A representation of the train-track-bridge coupling system

The most comprehensive and realistic model in the literature is the train-track-bridge system. The train subsystem is taken as the full vehicle model to make the operation more accurate. Track subsystem includes rail, sleeper and ballast. Bridges are generally modeled as Euler-Bernoulli beams. Although these three subsystems are independent, they strongly influence each other. Therefore, these subsystems will be briefly introduced in this section.

2.1. Train model

The 3D high speed train model proposed in this study is given in Fig. 1a and b. The train model under examination consists of two bogies, four wheels, a wagon, the primary suspension system linking the bogies and the wheels, and the secondary suspension systems connecting the bogies and the wagon. As seen in Table 1, each wheel has 3 DoFs in the high speed train model, while the car body and bogies each have 4 DoFs. Therefore, this study examines the high speed train model with 24 DoFs. Table 2 contains the parameters for the train model seen in Fig. 1. This study selects the train's direction of motion as the x-axis. The y-axis represents all vertical displacements, whereas the z-axis is employed to represent lateral displacements. The displacement and rotation movements are shown in Fig. 1a and b as r_{12} and Θ_{12}, respectively. Here, the first subscript denotes the train's components, such as the car body, the bogie, and the wheel, while the second denotes their direction, such as x, y, and z. While r_{cz} displays the lateral displacement of the car body, r_{cy} displays the vertical displacement. The front bogie's vertical and lateral displacement and the rear bogie's vertical and lateral displacement are represented by the symbols r_{b1y}, r_{b1z}, r_{b2y}, and r_{b2z}, respectively.

The vertical and lateral displacements of the front bogie's two wheelsets are denoted by the r_{w1y}, r_{w2y}, and r_{w1z}, r_{w2z}, respectively. The rear bogie's two wheelsets' vertical and lateral displacements are designated as r_{w3y}, r_{w4y}, and r_{w3z}, r_{w4z}, respectively.

The x-axis and z-axis, respectively, determine the train's rolling and pitching movements. The front bogie, the rear bogie, and the car body's pitching motion are each represented by the symbols Θ_{cz}, Θ_{b1z}, and Θ_{b2z}, respectively. The wheelsets, front bogie, rear bogie, and car body's rolling motion are each represented by the symbols Θ_{cx}, Θ_{b1x}, Θ_{b2x}, and Θ_{wx}, respectively. The car body mass, front and rear bogie masses, and wheel mass are each denoted by the parameters m_c, m_{b1}, m_{b2}, and m_w,

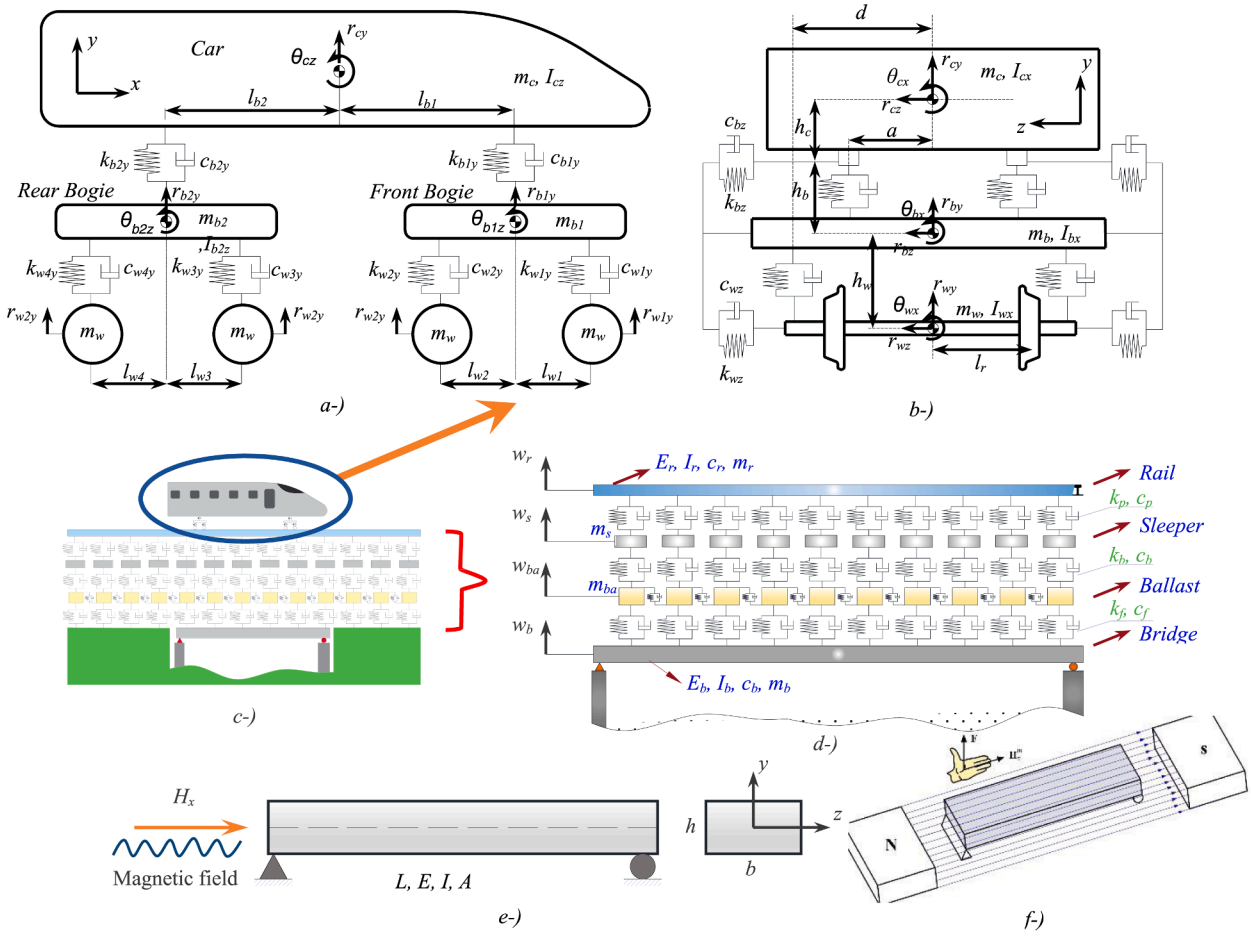

Fig. 1. Bridge beam and railway vehicle mathematical models in a horizontal magnetic field vector H_x. (a-) Side view (b-) Front view (c-) Illustration of TTBi (d-) Track-bridge couple model (e-) Beam in a horizontal magnetic field (f-) Application of magnetic field.

Table 1
Generalized coordinates of a full high-speed train model.

Parameter	Vertical motion	Lateral motion	Pitch motion	Roll motion
Car	r_{cy}	r_{cz}	θ_{cz}	θ_{cx}
Front bogie	r_{b1y}	r_{b1z}	θ_{b1z}	θ_{b1x}
Rear bogie	r_{b2y}	r_{b2z}	θ_{b2z}	θ_{b2x}
1st wheelset	r_{w1y}	r_{w1z}		θ_{w1x}
2nd wheelset	r_{w2y}	r_{w2z}		θ_{w2x}
3rd wheelset	r_{w3y}	r_{w3z}		θ_{w3x}
4th wheelset	r_{w4y}	r_{w4z}		θ_{w4x}

respectively. The car body, front bogie, and rear bogie's mass moment of inertia along the pitch axis are represented by the parameters I_{cz}, I_{b1z}, and I_{b2z}. I_{cx}, I_{b1x}, I_{b2x}, I_{wx} stand for the mass moment of inertia of the car body, the front and rear bogies, and the wheelsets, respectively, around the roll axis. The symbols l_{b1} and l_{b2} stand for the distance between the center of mass of the car body and the center of mass of the front bogie and the center of mass of the rear body, respectively. The distances between the center of the bogie mass and the front and back wheels are designated by the symbols l_{w1} and l_{w2}, respectively. The distances between the front wheel and the center of the rear bogie mass and between the rear wheel and the center of the rear bogie mass, respectively, are represented by l_{w3} and l_{w4}, respectively. The parameters k_{w1z}, k_{w2z}, k_{w3z}, and k_{w4z} indicate the lateral spring coefficient in the z-axis, whereas the parameters k_{w1y}, k_{w2y}, k_{w3y}, and k_{w4y} represent the vertical spring coefficient in the y-axis between the corresponding bogie and wheels.

Similar to how c_{w1z}, c_{w2z}, c_{w3z}, and c_{w4z} correspond to the lateral damping coefficient in the z-axis, respectively, and c_{w1y}, c_{w2y}, c_{w3y}, and c_{w4y} to the vertical damping coefficient in the y-axis. The vertical spring coefficient in the y-axis between the appropriate bogie and vehicle body is also represented by the parameters k_{b1y} and k_{b2y}. The vertical damping coefficient is represented by the symbols c_{b1y} and c_{b2y}. The lateral spring and damping coefficients in the z-axis are represented by the parameters k_{b1z} and k_{b2z}, respectively, and by c_{b1z} and c_{b2z}, respectively. v depicts the train's constant-velocity movement along the bridge beam from left to right. When modeling the train, the following presumptions are taken into account:

- As seen in Table 1, one car body and two bogies are modeled with 4-DOFs, and four wheelsets are modeled with 3-DOFs, which makes a total of 24-DOFs.
- The velocity of the vehicle, v, is constant along the track.
- The wheels of the train are always in touch with the rail.
- The wheelsets, bogies, and car body are recognized as rigid bodies.
- Euler-Bernoulli beam theory is used to simulate the rail and the bridge.
- The rail irregularity is not within the scope of this study and has been ignored.

2.2. Track and bridge model

In this paper, the dynamic system of the railway track and the bridge over which the 3D high-speed train moves at constant speed is given in Fig. 1d. The bridge and the rail are modeled separately as two simply supported uniform Euler-Bernoulli beams, while the ballast and sleeper are modeled as independent solid bodies. The sleeper, rail, ballast, and

Table 2
The parameters of the full 3D high-speed train.

Mass of train body (m_c)	40 tons	The secondary suspension system's lateral damping (c_{biz}, i=1,2)	10 kNs/m
Masses of front and rear bogies (m_{b1}=m_{b2})	3.04 tons	The primary suspension system's vertical damping (c_{wiy},i=1,2,3,4)	90.2 kNs/m
Wheels mass (m_{wi}, i=1,2,3,4)	1.78 tons	The primary suspension system's lateral damping (c_{wiz}, i=1,2,3,4)	10 kNs/m
Car mass moment of inertia in a pitch motion (I_{cz})	2080 tons m^2	Length of the bridge (L)	50 m
Car mass moment of inertia in a roll motion (I_{cx})	75 tons m^2	The longitudinal distance between car and bogie center of gravity (l_{bi},i=1,2)	8.75 m
Bogies mass moment of inertia in a pitch motion (I_{biz},i=1,2)	3.93 tons m^2	The longitudinal distance between bogie and vertical primary suspension (l_{wi}, i=1,2,3,4)	1.25 m
Bogies mass moment of inertia in a roll motion (I_{bix},i=1,2)	1.9 tons m^2	The vertical distance from bogie to lateral primary suspension (h_w)	0.22 m
Wheels mass moment of inertia in a roll motion (I_{wix}, i=1,2,3,4)	1.25 tons m^2	The vertical distance from car to lateral secondary suspension (h_c)	0.8 m
The secondary suspension system's vertical stiffness (k_{biy}, i=1,2)	1180 kN/m	The vertical distance from bogie to lateral secondary suspension (h_b)	0.5 m
The secondary suspension system's lateral stiffness (k_{biz}, i=1,2)	15,000 kN/m	Half of secondary suspension spacing (a)	1 m
The primary suspension system's vertical stiffness (k_{wiy}, i=1,2,3,4)	530 kN/m	Half of wheelset contact distance (l_r)	0.7175 m
The primary suspension system's lateral stiffness (k_{wiz}, i=1,2,3,4)	350 kN/m	Half of the primary spacing (d)	1 m
The secondary suspension system's vertical damping (c_{biy}, i=1,2)	39.2 kNs/m		

bridge motions are assumed to be only in the vertical direction and are represented by w_r, w_s, w_{ba}, and w_b, respectively. While E_r and E_b represent the modulus of elasticity of the rail and the bridge, the area moments of inertia are represented by I_r and I_b. Similarly, the damping coefficients of the beams are represented by c_r and c_b, while the masses of the unit length of the beams are represented by μ_r and μ_b. Also, m_s and m_{ba} stand in for the sleeper and ballast masses. The spring and damping coefficient between rail and sleeper are represented by k_p and c_p, respectively, while spring and damping coefficient between sleeper and ballast are represented by k_b and c_b. In addition, the coefficient of the spring and damping between the ballast and the bridge are defined as k_f and c_f, and their values are given in Table 3.

3. Motion equations of train-track-bridge system with the magnetic field

This section is devoted to presenting the basic equations describing the mathematical model of the bridge modeled as a simply supported Euler Bernoulli beam and subjected to a magnetic field. In this study has considered a simple supported Euler-Bernoulli steel bridge beam with the track structure subjected to the magnetic field. The magnetic field effect has been integrated into the equation of the TTBi model using Maxwell's equations, which was studied before some researchers gave in [66,69,73]. According to this, the parameters related to the current density vector (J), magnetic field vector (h), electric field vector (e), magnetic field permeability (η), and magnetic field intensity (H) can be obtained as follows:

$$J = \nabla \mathrm{x} \boldsymbol{h},\ \nabla \mathrm{x} e = -\eta \frac{\partial \boldsymbol{h}}{\partial t},\ \nabla . \boldsymbol{h} = 0 \tag{1}$$

$$e = -\eta \left(\frac{\partial \mathrm{U}}{\partial t} \mathrm{x} \boldsymbol{H} \right),\ \boldsymbol{h} = \nabla \mathrm{x} (\mathrm{U} \mathrm{x} \boldsymbol{H}) \tag{2}$$

The symbols ∇ and t represent the Laplace operator and time, respectively. On the other hand, displacement field vector U is defined as $= u\vec{\mathrm{i}} + v\vec{\mathrm{j}} + w\vec{\mathrm{k}}$. Considering that the Euler-Bernoulli beam studied in this study bending only vertical direction, so magnetic field vector can be stated as follow:

$$\boldsymbol{h} = \boldsymbol{H}_x \frac{\partial w}{\partial x} \vec{\boldsymbol{k}} \tag{3}$$

The Lorentz force applied to any structure in the magnetic field is defined as follows, considering the current density vector given in Eq. (4) [65,66]:

$$f_{mz} = f_{mz} \vec{k} = \eta (\boldsymbol{J} \mathrm{x} \boldsymbol{H}) = \eta \left[H_x^2 \left(\frac{\partial^2 w}{\partial x^2} + \frac{\partial^2 w}{\partial z^2} + \frac{\partial^2 w}{\partial y \partial z} \right) \vec{k} \right] \tag{4}$$

Considering Galerkin functions given in Eqs. (11a–c) and (12), the Lorentz force (F_l) is expressed as follows [74]:

$$F_l = \int_{-h/2}^{h/2} f_{mz} d_z = \eta h H_x^2 \left(\sum_{i=1}^{n} \varphi''_i(x) q_i(t) \right) \tag{5}$$

The parameter h given in the above equation represents the height of the cross-section area. To investigate the magnetic field upon the bridge, track substructures, and train, the following dimensionless parameter is determined:

$$H_x^m = \frac{\eta h H_x^2 L^2}{D_b},\ D_b = \frac{E h^3}{12(1-\upsilon^2)} \tag{6}$$

Here H_x^m represents the magnetic field intensity parameter, L represents the length of the beam, and E represents the modulus of elasticity of the beam. The poisson ratio of the material for the substructure is represented by the parameter υ.

The motion equations of the TTBi system given in Fig. 1 are obtained

Table 3
The parameter of the track and beams parameter.

	Beam Parameter			Track Parameter			
	Rail	Right Bridge	Left Bridge				
Elasticity module (GPa)	210	207	200	Mass of sleeper (kg)	237	Mass of ballast (kg)	683
Cross-section inertia moment (m^4)	0.174	0.2	0.2	The stiffness coefficient between the rail and the sleeper (N/m)	1.2 × 10^8	The damping coefficient between the rail and the sleeper (Ns/m)	1.24 × 10^5
Mass of unit length (kg/m)	52.5	20,000	18,000	The stiffness coefficient between the sleeper and the ballast (N/m)	2.4 × 10^8	The damping coefficient between the sleeper and the ballast (Ns/m)	5.88 × 10^4
Equivalent damping coefficient (Ns/m)	1750	1750	1750	The stiffness coefficient between the ballast and the bridge (N/m)	6.5 × 10^7	The damping coefficient between the ballast and the bridge (Ns/m)	3.12 × 10^4

using the Lagrangian method all equations are given in the Appendix C.

4. Results and discussion

It is essential to verify the solution method presented in this study with previous studies in the literature to evaluate the results of the magnetic field applied to bridge and train interaction analysis more consistently. For the study results to be understood as acceptable, the validation results should be very similar to each other. In this section, firstly, the solving method is verified, and then the dynamic responses of the TTBi system are examined in detail.

4.1. Validation

The motion equations for the entire system are first generated using the Lagrangian approach to conduct the dynamic analysis of the model considered in this paper. The bridge system comprises eight differential equations and a total of 56 2nd order equations of motion, whereas the train and track each have 24 differential equations. The state-space form provided in Appendix B condenses these resulting equations into 112 first-order differential equations. These equations are solved more precisely and quickly using the fourth-order Runge-Kutta method.

The simpler 4 DoFs quarter railway car and bridge model shown in Fig. 2 is used to evaluate the sophisticated and multi-DoF train-track-bridge model shown in Fig. 1. The validation example uses a model that has been researched by Yang and Sun and is well-known in the literature. The quarter car model with 4 DoFs has two wheels and one bogie. The parameters used in both the model used to evaluate the validity of this study and the model depicted in Fig. 2 are identical. A simple-supported beam model of the bridge has the following specifications: L= 30 m, I= 0.175 m^4, E= 27.5 GPa, μ= 1000 kg/m. The properties of a quarter railway vehicle model are as follows: M_v=1500 kg, I_v=2738 kgm^2, k_{w1}=k_{w2}=85 kN/m, c_{w1}=c_{w2}=0, M_{w1}=M_{w2}=15 kg, d=2.5 m, and constant vehicle velocity v=5 m/s [10].

The comparison of the dynamic behavior of the four degrees of freedom model shown in Fig. 2 is shown in Fig. 3. In contrast to the reference research, which employed the Newmark-β method to solve the system's motion equations, this study made use of the Runge-Kutta technique. Additionally, although Δt = 0.001 sec was used for the solution time interval in the previous investigation, Δt = 0.01 s was used in this study. The findings show that, even if there is a coarse time interval, the dynamic reactions of the vehicle when utilizing the solution approach suggested in this paper are almost identical to those of the study published in the literature.

Additionally, a simply supported micro beam with L=10 nm, previously studied in the literature by [69], was analyzed to confirm the modeling and compare it to the literature. The results presented in this study, as shown in Table 4, are compatible with the literature's solutions [69].

4.2. Responses of different train velocity

The parameters of the track and especially the bridge that high-speed trains pass over are crucial. Although the train-track-bridge is a different subsystem, they strongly influence each other. The high-speed trains vibrate the bridge over which they pass through the track, and the vibrating bridge affects the structure on the bridge, especially the train. The train's speed causes the bridge to vibrate at a specific frequency. The speed of the train corresponding to these determined frequencies is called the critical speed. This study considers the first four vibration modes of the bridge. Eq. (7) provides the computation of the beam's natural frequency [2], which stands for the beam's circular natural frequency.

$$\omega_j^2 = \frac{j^4\pi^4 EI}{\mu L^4}(\mathrm{rad}/\mathrm{s}), \tag{7}$$

The circular natural frequency of the beam is provided in Eq. (7). The frequency of the beam vibration is determined in Eq. (8).

$$f_j = \frac{\omega_j}{2\pi} = \frac{j^2\pi}{2L^2}\sqrt{\frac{EI}{\mu}}(Hz) \tag{8}$$

The first four vibration modes of the right and left bridge beams may be estimated using Eq. (8), as shown in Table 5. Speed parameters are the natural frequency (f_b) ratio of the bridge and the force-frequency (f_v) of the train. Resonance happens when f_v and f_b are equivalent. The train going over the bridge experiences an increase in the periodic motion amplitude due to the resonance. The train length is the most critical characteristic for the resonance induced by the train passing over the bridge beam [75]. Eq. (9) [76] gives the critical velocity of the train-track-bridge scenario that causes resonance.

$$V_{cr,j} = \frac{df_{b,j}}{i} \tag{9}$$

In Eq. (9), v_{cr} stands for the train's critical velocity, and $f_{b,j}$ for the bridge beam's natural frequency. The symbol d represents the separation between the front and back wheels of the front and rear bogie. i is represented as the half oscillation cycle number [77,78]. Using Table 2, the length d is computed as l_{b1}+l_{b2}+l_{w1}+l_{w4}=20 m. As a result, the critical train velocities for the bridge's first four modes are established, as shown in Table 5.

The dynamic responses of the high-speed train are investigated by

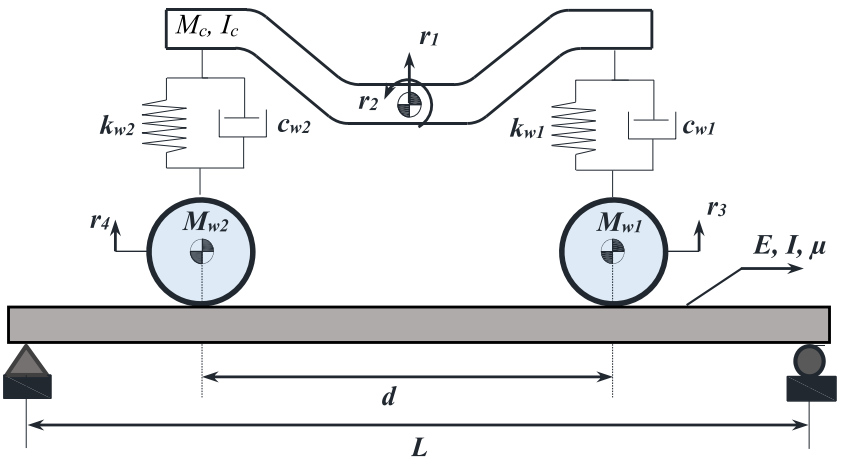

Fig. 2. Model of validation for the reliability of the research's methodology.

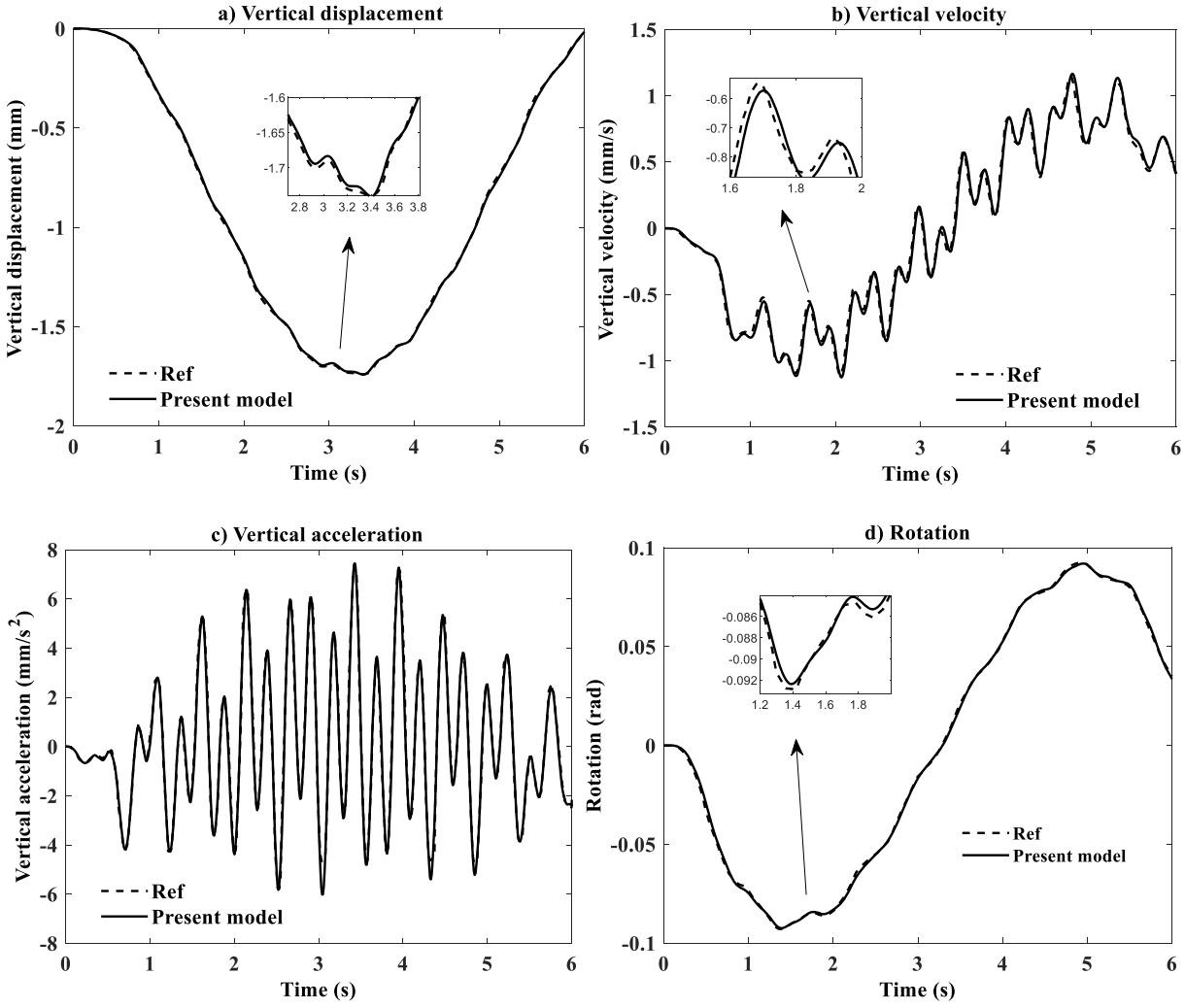

Fig. 3. Comparisons of the train body's dynamic responses, where a 4 DOF quarter-railway model is used and the dynamic responses of the bogie are compared. The dashed line represents the result of the reference work, and the solid line the present work a) Displacement of bogie in vertical direction b) Velocity of bogie in vertical direction c) Acceleration of bogie in vertical direction d) Rotation of the bogie.

Table 4
For different dimensionless magnetic field intensities H_x^m, the first three frequency parameters; $\lambda_i = \omega_i L^2\sqrt{\rho A/EI}$.

		λ_1	
H_x^m $*10^{-6}$	$\eta h H_x^2(nN/m)$	Ref. [69]	Present study
0	0.0000	9.86310	9.5296
1	58.6081	164.8512	164.7532
3	175.8242	285.1898	285.2505
5	293.0403	368.0904	368.1256
7	410.2564	435.4858	435.8915

Table 5
The critical velocity of the associated train-track-bridge system and the first four vibration mode frequencies of the right and left bridge beams.

Mod Num.	1	2	3	4
Right Bridge Beam L=50 m				
f (Hz)	0.91	3.62	8.14	14.46
v_{cr} (m/s)	18.08	72.32	162.72	289.28
Left Bridge Beam L=50 m				
f (Hz)	0.94	3.75	8.43	14.99
v_{cr} (m/s)	18.73	74.93	168.59	299.72

considering the train-bridge system's second critical speed, v_{cr}. In the analyzes, the train velocities are v=0.1, 0.25, 0.5, and 1v_{cr}, and the bridge is in a magnetic field effect. The dimensionless magnetic field intensity is applied in all analyzes as H_x^m=0, 5, 10, 20, 30. In the graphs, the horizontal axis is the dimensionless time *x(t)/L*, which indicates the position of the high-speed train relative to the bridge.

Figs. 4 and 5 show, respectively, the train body's vertical displacement and vertical acceleration. The figures show that the high-speed train's dynamic reactions are strongly influenced by the train's speed and the intensity of the magnetic field. Examining Fig. 4, when the magnetic field intensity rises, the vertical displacement of the train decreases. For example, H_x^m=0, that is, when no magnetic field is applied to the bridge, the maximum value of the train's vertical displacement is -0.0156, -0.0189, -0.0212 and -0.0234 m if the train speed is 0.1v_{cr}, 0.25v_{cr}, 0.5v_{cr} and v_{cr}, respectively. When H_x^m=30, the maximum value of the train's vertical displacement is -0.0083, -0.0095, -0.0091, and -0.0145 m in case the train speed is 0.1v_{cr}, 0.25 v_{cr}, 0.5v_{cr} and v_{cr}, respectively. In other words, with the increase in the magnetic field intensity applied to the bridge, it is seen that the maximum displacement of the train body decreases by 48% on average. In addition, as the train speed increases, the maximum vertical displacement is further away from the starting position of the bridge. For example, in Fig. 4a–c, the train's maximum vertical displacement value is when the train is on the bridge, while in Fig. 4d, this value occurs after the train leaves the

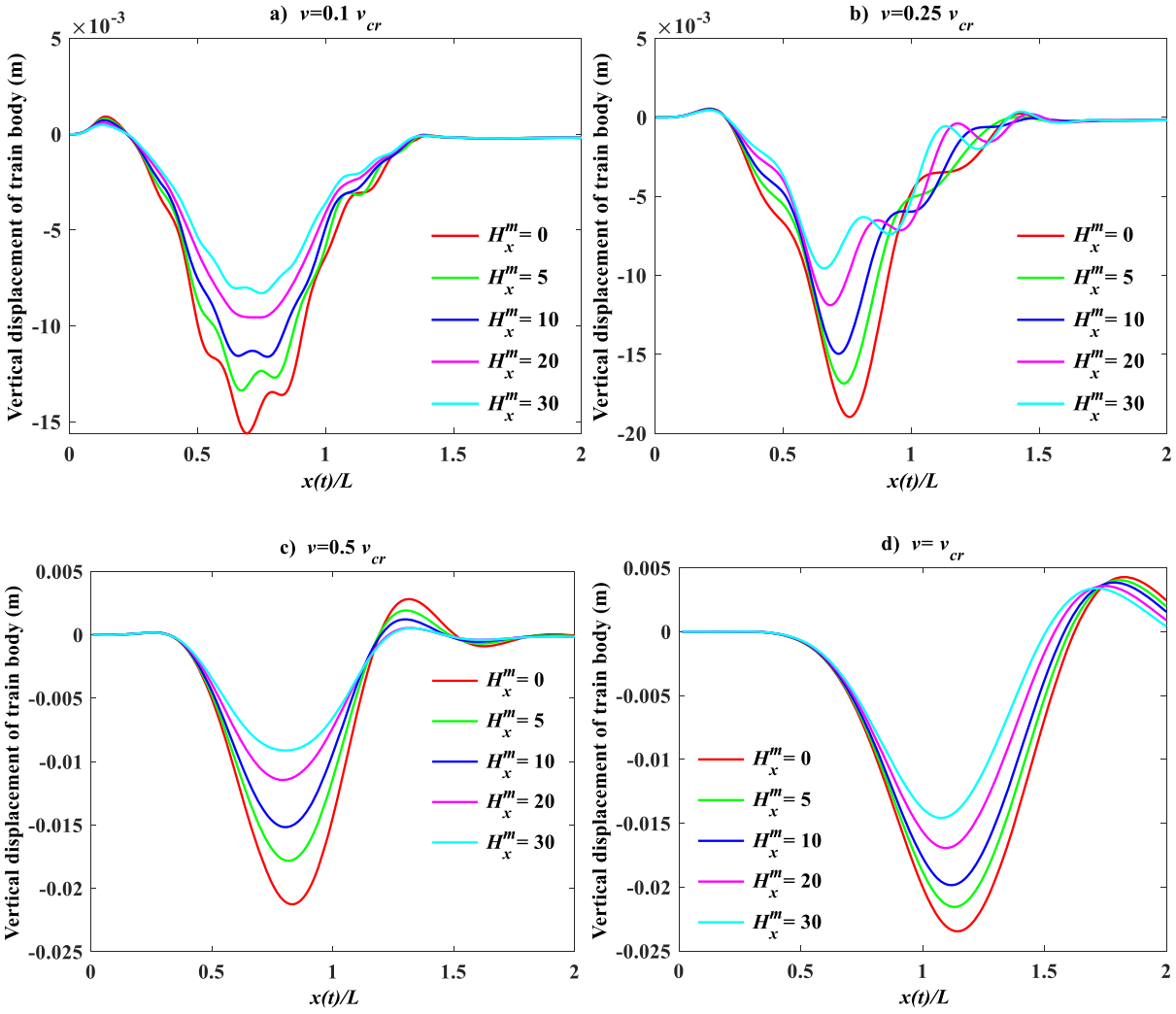

Fig. 4. Time dependant response of the vertical displacement of train body for various dimensionless magnetic field intensity H_x^m=0, 5, 10, 20, 30. (a) v=0.1v_{cr} (b) v=0.25v_{cr} (c) v=0.5v_{cr} (d) v=v_{cr}; for dimensionless time $x(t)/L$, L=50 m, where the analysis results of the full train model with the track at four different speeds and five different dimensionless magnetic field intensities are given in colour graphics. Here, the graph H_x^m=0 is represented in red, the graph H_x^m=5 in green, the graph H_x^m=10 in blue, the graph H_x^m=20 in magenta, and the graph H_x^m=30 in cyan.

bridge. The time during which the maximum amplitudes also differs according to the magnetic field intensity. Especially in Fig. 4b and d, as the magnetic field intensity increases, the maximum vertical displacement of the train appears to be where the bridge is closer to the initial reference. It is known that the magnetic field's intensity affects the frequency of the bridge beam's natural vibration.

When the train body's vertical acceleration in Fig. 5 is analyzed, as in the previous graph, the maximum acceleration decrease as the magnetic field intensity increases. For instance, when H_x^m=0, the root mean square (RMS) of the vertical acceleration of the train are 0.0089, 0.0409, 0.1172 and 0.328 m/s^2 if the train speed is 0.1v_{cr}, 0.25v_{cr}, 0.5v_{cr} and v_{cr}, respectively. When H_x^m=30, the RMS value of the vertical acceleration of the train becomes 0.0034, 0.0375, 0.0463, and 0.231 m/s^2 if the train speed is 0.1v_{cr}, 0.25v_{cr}, 0.5v_{cr}, and v_{cr}, respectively. As a result, the acceleration values decrease as the magnetic field intensity applied to the steel bridge increases. In Fig. 5a, when the magnetic field is applied, the RMS of the acceleration value decreases by 61.8%, while it decreases by 8, 60, and 29% in Fig. 5b, Fig. 5c, and Fig. 5d, respectively. It is seen that the decrease in Fig. 5b and Fig. 5d is smaller than the others. This is because v_{cr} =72.32 m/s is considered the second critical speed in this study. Since the train speed is at the crucial speed in Fig. 5d, the vertical acceleration values are high even if the magnetic field is applied. In Fig. 5b, the train speed is 0.25v_{cr}, and since this speed is close to the first critical speed according to Table 5, the acceleration values in this graph did not decrease much due to the magnetic field application. It is understood from this that if the train speed moves at critical speeds, even in the case of applying a magnetic field, the maximum dynamic responses are high. However, if the train speed is outside of the critical speeds, the dynamic responses are considerably reduced if a magnetic field is applied.

Similarly, as the train's speed increases, it is seen that the maximum vertical acceleration value is further away from the reference position of the bridge. Also, in the case of the maximum magnetic field effect, when the train speed is 0.5 v_{cr}, the maximum vertical acceleration value of the train is 0.078 m/s^2, while if the train speed is v_{cr}, it is 0.522 m/s^2. In other words, resonance occurs since the train is at the critical speed of the train-bridge system, and the maximum acceleration value increases approximately seven times.

In Figs. 6 and 7, the pitch and roll motion of the train is examined in the case of different magnetic field intensities and four different train speeds, v=0.1, 0.25, 0.5, and 1v_{cr}. When Fig. 6–c are examined carefully; it is seen that the pitch motion of the train is almost similar regardless of the train speed, while the pitch motion of the train is relatively high in Fig. 6d compared to the other graphs. In addition, with the increase of

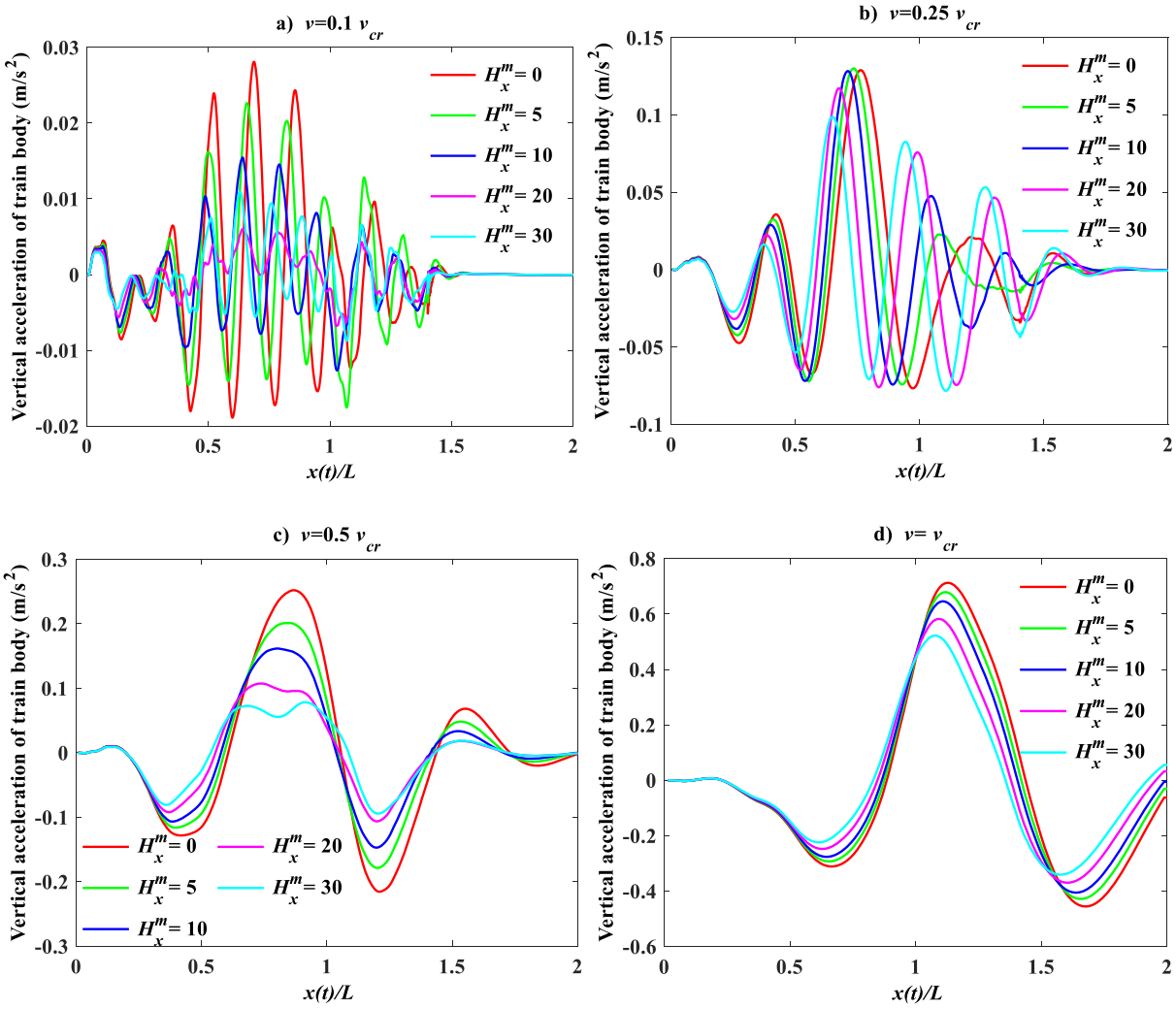

Fig. 5. Time dependant response of the vertical acceleration of train body for various dimensionless magnetic field intensity H_x^m=0, 5, 10, 20, 30. (a) v=0.1v_{cr} (b) v=0.25v_{cr} (c) v=0.5v_{cr} (d) v=v_{cr}; for dimensionless time $x(t)/L$, L=50 m, where the analysis results of the full train model with the track at four different speeds and five different magnetic field intensities are given in colour graphics. Here, the graph H_x^m=0 is represented in red, the graph H_x^m=5 in green, the graph H_x^m=10 in blue, the graph H_x^m=20 in magenta, and the graph H_x^m=30 in cyan.

magnetic field effect in Fig. 6d, it is seen that the pitch motion of the train decreases considerably to other graphs. For example, when the magnetic field is not taken into account, the maximum pitch motion of the train body is 11.8 $\times$ 10^{-4} rad, while it is 4.4 $\times$ 10^{-4} rad when the dimensionless magnetic field intensity is H_x^m=30.

When the roll motion of the train body given in Fig. 7 is examined, unlike the previous graphs, the maximum roll motion decreases as the train speed increases. Another important detail is that in Fig. 7a–c, the magnetic field intensity does not significantly change the roll motion, while in Fig. 7d when the magnetic field intensity increases, the roll motion of the train decreases considerably. This is because in Fig. 7d if the train is at the critical speed and in the absence of magnetic field intensity, the roll motion is relatively high. In other words, in the case of a railway bridge exposed to the magnetic field effect, even if the vehicle moves at critical speeds, it can considerably decrease the train's dynamic response.

Fig. 8 shows the displacement of the bridge's midpoint in the case of four different velocities and five different magnetic field intensities. In the given graphs, the horizontal axis shows the dimensionless time as in the previous graphs. On the other hand, the vertical axis shows the maximum vertical dimensionless displacement of the bridge midpoint as the dynamic amplification factor (DAF). Here, it can be expressed with the formula DAF=$w_{max(L/2,t)}/w_{st}$, and also, the expression specified as w_{st} in the formula is the static displacement value of the middle point of the bridge due to the train mass and is determined by the formula w_{st}=$FL^3/48EI$. When Fig. 8 is examined, the value and time of the maximum displacement of the bridge midpoint increase as the train speed increases. In Fig. 8d, when the magnetic field intensity is zero, the maximum DAF value of the bridge midpoint is 1.32, while if the magnetic field intensity is H_x^m=30, the maximum DAF value is 0.72. In other words, as it approaches the critical speed, DAF exceeds 1, and DAF decreases with increasing magnetic field intensity.

4.3. Effect of variable train velocity

In Figs. 9–11, the displacement of the railway bridge's midpoint and the train body's dynamic responses are given when the train speed changes in the range of 1/v_{cr} from 0 to 2v_{cr}. The speed parameter is given as μ=v/v_{cr} in the graphs. The train's maximum vertical displacement and acceleration occurred at critical speeds, as shown in Fig. 9. Also, the maximum vertical displacement is reduced by half in the presence of the magnetic field. There are peaks in two different places according to the train body's maximum vertical displacement and acceleration. These occurred where the velocity parameter is close to μ=0.25 and μ=1.

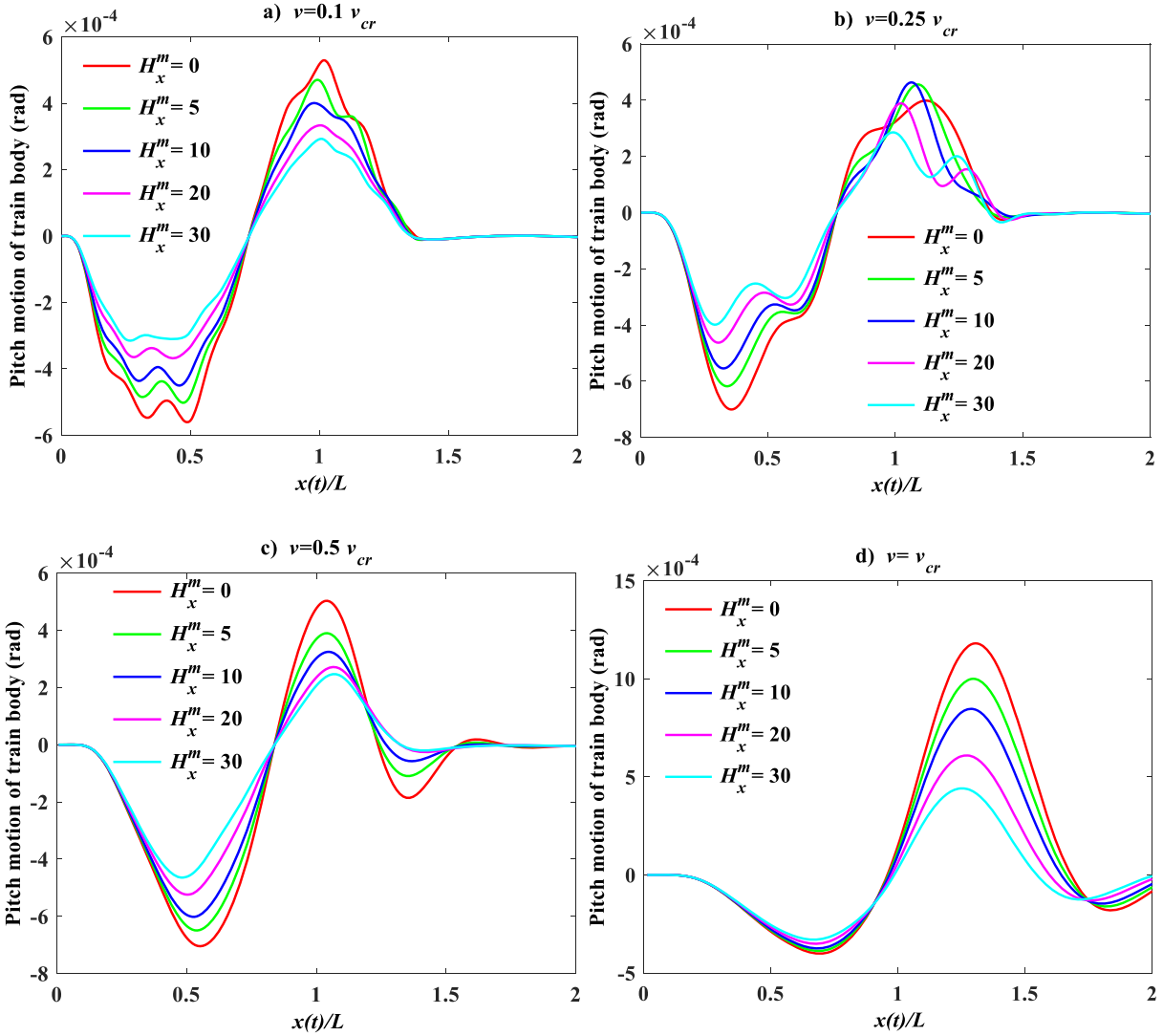

Fig. 6. Time dependant response of the pitch motion of train body for various dimensionless magnetic field intensity H_x^m=0, 5, 10, 20, 30. (a) v=0.1v_{cr} (b) v=0.25v_{cr} (c) v=0.5v_{cr} (d) v=v_{cr}; for dimensionless time $x(t)/L$, L=50 m, where the analysis results of the full train model with the track at four different speeds and five different magnetic field intensities are given in colour graphics. Here, the graph H_x^m=0 is represented in red, the graph H_x^m=5 in green, the graph H_x^m=10 in blue, the graph H_x^m=20 in magenta, and the graph H_x^m=30 in cyan.

According to Table 5, It can be observed that these speed parameters are quite near to the system's first two critical speeds. In addition, according to Fig. 9, if the magnetic field intensity increases, the maximum displacement and acceleration values decrease, and the velocity parameter increases at that moment. For example, in Fig. 9a, while the maximum displacement value of the train body is 0.029 m at μ=0.79 for H_x^m=0. This value is 0.0165 m at μ=1.05 for H_x^m=30. When Fig. 9b is examined, in case of an increase in magnetic field intensities, the maximum acceleration values increase but occur at a higher speed parameter. It is understood that the magnetic field intensity increases the critical speeds of the train-bridge system by changing the vibration characteristics of the bridge through which the train passes.

In Fig. 10, the roll and pitch motions of the train body are given according to five different dimensionless magnetic field intensities. In Fig. 10a, the pitch motion peaked in two different places as in the previous graphs; these values are pretty near to the train-bridge system's critical speeds. Similarly, as the dimensionless magnetic field intensity increases, while the maximum pitch motion decreases by half, the velocity parameter at which it occurs also increases. In Fig. 10b, while the roll motion is relatively high at low train speeds, it suddenly decreases as the speed increases and then takes its almost constant value. In addition, in the presence of a dimensionless magnetic field, the roll motion of the train body is reduced by a minimal amount. The most significant displacement of the railway bridge's midpoint, modeled using the Euler-Bernoulli beam theorem and subjected to five different dimensionless magnetic field strengths as H_x^m=0, 5, 10, 20, and 30 are shown in Fig. 11.

According to the graph, the bridge beam's vibration amplitudes decrease as the magnetic field intensity rises, and it behaves as if it were a more rigid bridge. In addition, in the absence of magnetic field intensity, the maximum DAF value of the bridge beam is at μ=0.9 and exceeds 1.3, while in the case of the maximum magnetic field intensity, the DAF value is at μ=1.27 and 0.73. In other words, with magnetic field intensity, the bridge beam's natural frequencies increase, and the critical speeds of the train-bridge system increase. Additionally, it can be shown that increasing stiffness reduces the bridge beam's vibration amplitudes.

4.4. *Effect of random track irregularity*

Until this part of the paper, there is no irregularity in the system, and it has been neglected. In this section, the responses in the case of a track irregularity and the bridge in the magnetic field will be examined. The

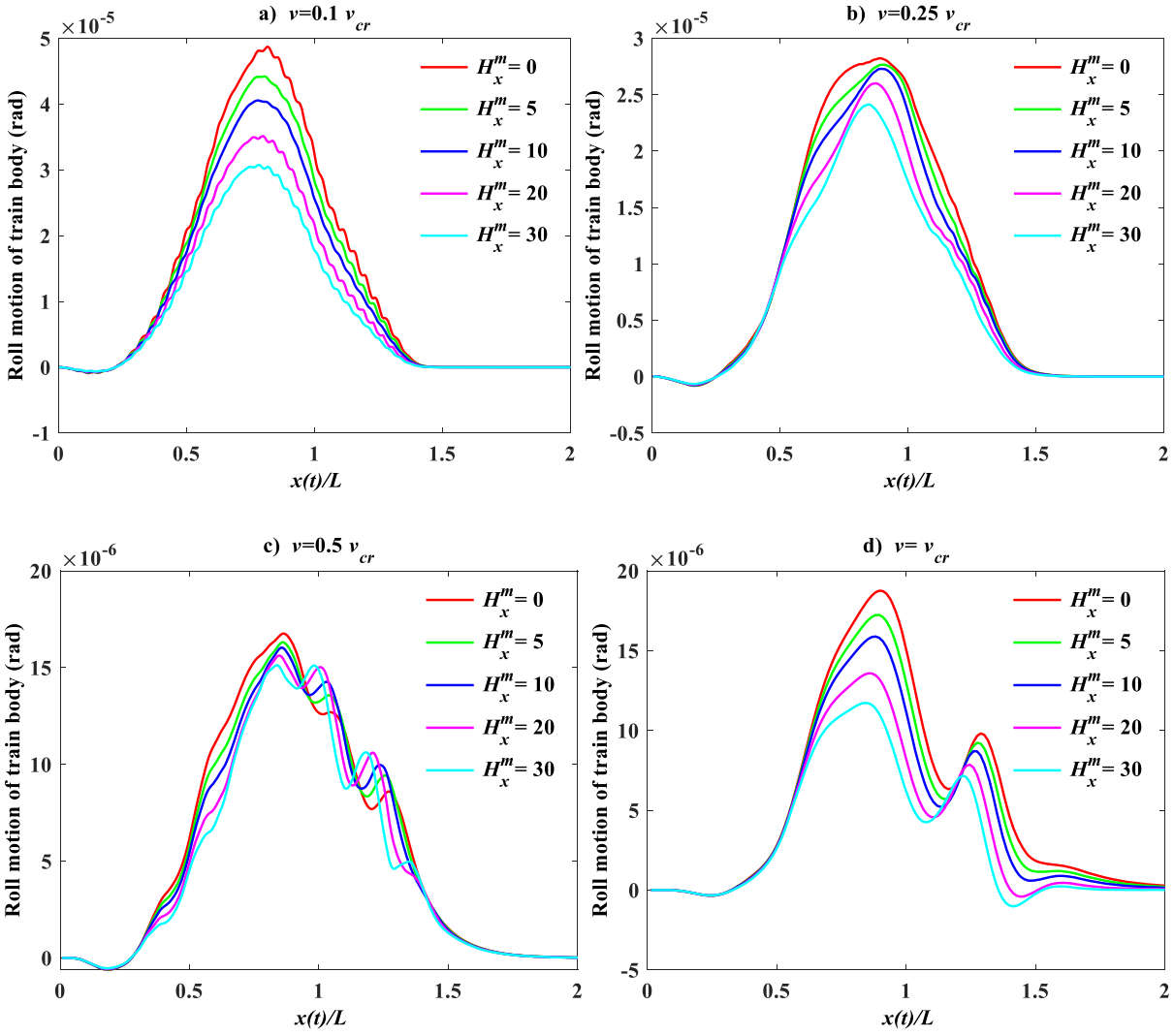

Fig. 7. Time dependant response of the roll motion of train body for various dimensionless magnetic field intensity H_x^m=0, 5, 10, 20, 30. (a) v=0.1v_{cr} (b) v=0.25v_{cr} (c) v=0.5v_{cr} (d) v=v_{cr}; for dimensionless time $x(t)/L$, L=50 m, where the analysis results of the full train model with the track at four different speeds and five different magnetic field intensities are given in colour graphics. Here, the graph H_x^m=0 is represented in red, the graph H_x^m=5 in green, the graph H_x^m=10 in blue, the graph H_x^m=20 in magenta, and the graph H_x^m=30 in cyan.

track irregularities are known as secondary sources of bridge vibrations, the primary source of bridge vibrations being train vibrations. Track irregularities can be investigated in the random category and created with the inverse Fourier transform as follows [79].

$$r(x) = \sum_{k=1}^{N} \sqrt{4A_r(\omega_k/\omega_o)^{-2}\Delta\omega}\cos(\omega_k x - \varphi_k) \tag{10}$$

Here $r(x)$ represents the irregularity profile, A_r is a magnitude parameter. ω_k=k$\Delta\omega$ and ω_o=1/2π represent the number of waves and frequency of discontinuity, respectively. $\Delta\omega$, frequency increment, x represents the position of the train relative to the bridge, and φ_k represents a random number generated between 0 and 2π. N denotes the total number of terms used to calculate rail surface roughness. The independent right and left track irregularity obtained from these data are given in Fig. 12.

The obtained track profile is added to the $w_b(x,t)$ formula, which represents the vertical movement of the rail in the energy equations of the TTBi system in Appendix A, as in the equation below. In this case, the beam displacement, velocity, and acceleration equations are given as follows.

$$y = w_b(x,t) + r(x) \tag{11}$$

$$\frac{dy}{dt} = \frac{\partial w_b}{\partial x}\frac{dx}{dt} + \frac{\partial w_b}{\partial t} + \frac{dr}{dx}\frac{dx}{dt} \tag{12}$$

$$\frac{d^2y}{dt^2} = \frac{\partial^2 w_b}{\partial x^2}\left(\frac{dx}{dt}\right)^2 + 2\frac{\partial^2 w_b}{\partial x \partial t}\frac{dx}{dt} + \frac{\partial^2 r}{\partial x^2}\left(\frac{dx}{dt}\right)^2 + \frac{\partial w_b}{\partial x}\frac{d^2x}{dt^2} + \frac{\partial^2 w_b}{\partial t^2} + \frac{dr}{dx}\frac{d^2x}{dt^2} \tag{13}$$

Fig. 13 shows the dynamic displacement and acceleration of the train in the vertical direction as it crosses the bridge in the case of both track irregularity and five different dimensionless magnetic field intensities. When the figure is examined, the dynamic displacement is almost the

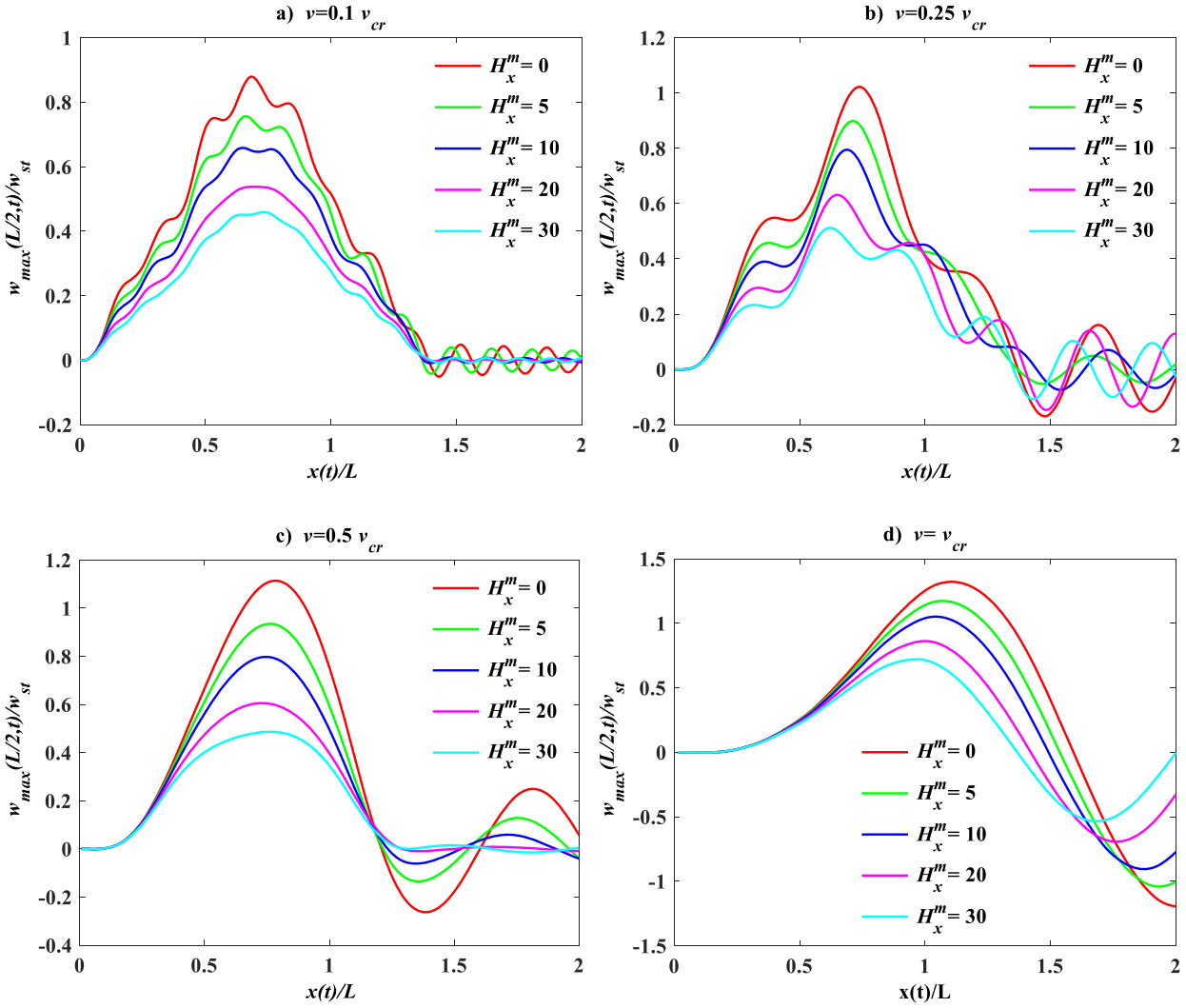

Fig. 8. Time dependant response of the midpoint of bridge beam for various dimensionless magnetic field intensity H_x^m=0, 5, 10, 20, 30. (a) v=0.1v_{cr} (b) v=0.25v_{cr} (c) v=0.5v_{cr} (d) v=v_{cr}; for dimensionless time $x(t)/L$, L=50 m, where the analysis results of the full train model with the track at four different speeds and five different magnetic field intensities are given in colour graphics. Here, the graph H_x^m=0 is represented in red, the graph H_x^m=5 in green, the graph H_x^m=10 in blue, the graph H_x^m=20 in magenta, and the graph H_x^m=30 in cyan.

same as the graph in Fig. 4d, where there is no track irregularity. However, when the graph is examined carefully, it is seen that there is a fluctuation in the displacement of the train body at about 0.5 and around the dimensionless time in Fig. 13a. The same situation occurs in regions where dimensionless time is 1.8. In addition, thanks to the magnetic field applied to the bridge, vertical displacements in this figure can be reduced considerably. When the vertical acceleration of the train body is examined in Fig. 13b, it is seen that the acceleration graph is quite different from the one in Fig. 5d in the case of random track irregularity. For example, when H_x^m=0, the RMS (root mean square) of the acceleration in Fig. 5d is 0.1384 m/s^2, while the RMS of the graph in Fig. 13b is 0.3665 m/s^2 in case of track irregularity. In other words, when the irregularity is applied to the system, as in Fig. 12, the RMS of the acceleration of the train body increases approximately 2.6 times. As the dimensionless magnetic field intensity increases, the vertical acceleration of the train body can be partially reduced.

When the pitch and roll movements of the train body are examined in Fig. 14, it is seen that the movements of the train body are highly affected when there is track irregularity. For example, according to Fig. 6d, when H_x^m=0, and there is no irregularity in the system, the maximum pitch movement of the train body was 1.18 $\times$ 10^{-3}. In contrast, when there was an irregularity, the maximum pitch movement was 1.35 $\times$ 10^{-3} and increased by about 15%. In Fig. 14b, the roll motion of the train body is heavily affected by the track irregularity, and the effect of the magnetic field intensity is almost unclear. For example, according to Fig. 7d, the maximum roll movement of the train body is 1.87 $\times$ 10^{-5}, while in Fig. 14b, this value is 3.28 $\times$ 10^{-4}. In other words, in the case of track irregularity, the maximum roll motion of the train body increases approximately 17.5 times.

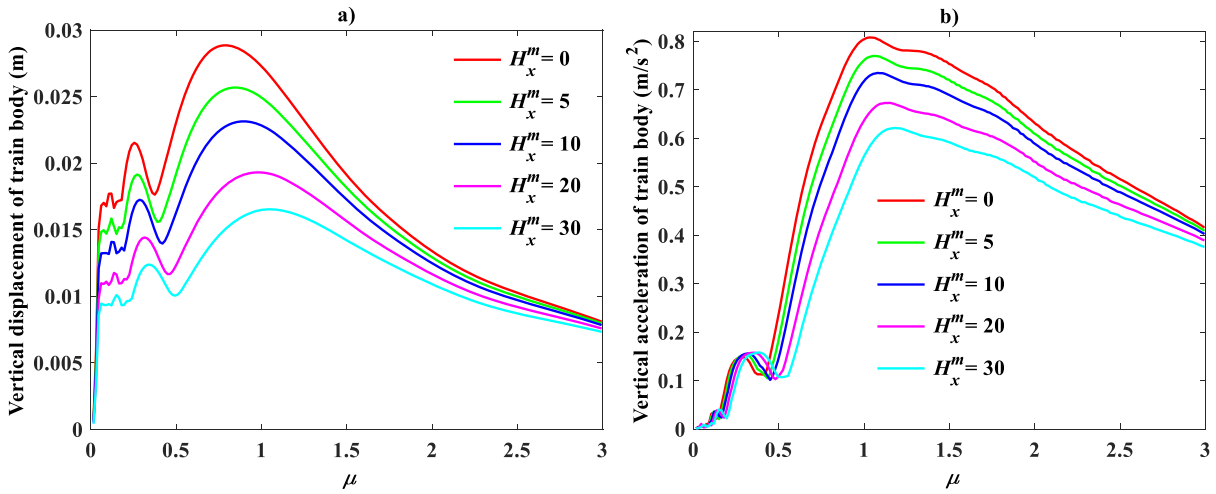

Fig. 9. Velocity dependant change of the maximum displacement of train body for various dimensionless magnetic field intensity H_x^m=0, 5, 10, 20, 30. (a) Vertical displacement of train body (b) Vertical acceleration of train body, where the analysis results of the full train model with the track at speed parameter μ between 0 and 3, and five different magnetic field intensities and when it passes over a 50 m long bridge are given in colour graphics. Here, the graph H_x^m=0 is represented in red, the graph H_x^m=5 in green, the graph H_x^m=10 in blue, the graph H_x^m=20 in magenta, and the graph H_x^m=30 in cyan.

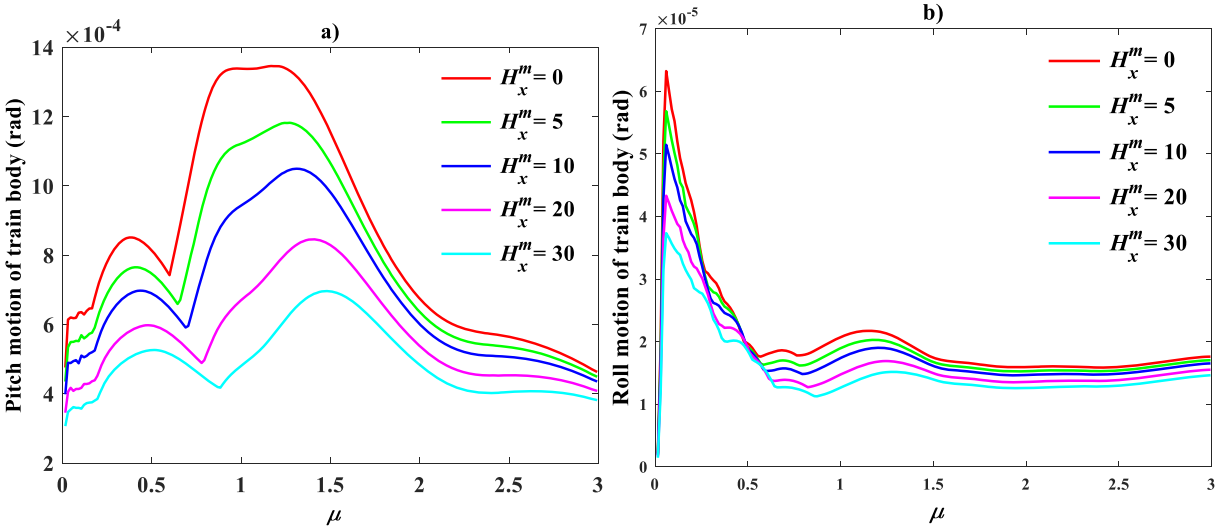

Fig. 10. Velocity dependant change of the maximum pitch motion of train body for various dimensionless magnetic field intensity H_x^m=0, 5, 10, 20, 30. (a) Pitch motion of train body (b) Roll motion of train body, where the analysis results of the full train model with the track at speed parameter μ between 0 and 3, and five different magnetic field intensities and when it passes over a 50 m long bridge are given in colour graphics. Here, the graph H_x^m=0 is represented in red, the graph H_x^m=5 in green, the graph H_x^m=10 in blue, the graph H_x^m=20 in magenta, and the graph H_x^m=30 in cyan.

5. Conclusion

In this study, a high-speed train with 24 degrees of freedom operating in a magnetic field interacts dynamically with a simply supported railway bridge that can be described using the Euler-Bernoulli beam theorem. The high-speed train is modeled in 3D, and the track structure between the train and the bridge is also considered. In this manuscript, the bridge beam is in the magnetic field effect in the horizontal direction, and the Lorentz force in the vertical direction due to this effect is included in the motion equation of the bridge beam. The motion equations of the examined train-track-bridge model are obtained using the Lagrangian method, and then with the use of state-space forms, these equations are reduced to first-order differential equations. The dynamic behaviors of the railway bridge and train body exposed to different magnetic field intensities are examined in detail using the fourth-order Runge-Kutta method.

In general, it has been observed that the magnetic field intensity applied to the railway bridge significantly affects the dynamic behavior of the train. Because when the magnetic field intensity applied to the bridge beam in the axial direction is increased, the induced Lorentz force increases, and the movement of the beam in the magnetic field becomes stiffer. Therefore, the beam begins to behave more rigidly, and its natural frequency increases. An increase in the natural frequency means a further away from the critical region. Thus, the dynamic displacements of the beam and the train are reduced due to increased beam stiffness and deviation from the critical velocity. For instance, it was observed that the vertical displacement of the train body decreased considerably after applying a magnetic field to the railway bridge. For example, in Fig. 4, if the dimensionless magnetic field coefficient increases from H_x^m=0 to H_x^m=60, the displacement of the train body in the vertical

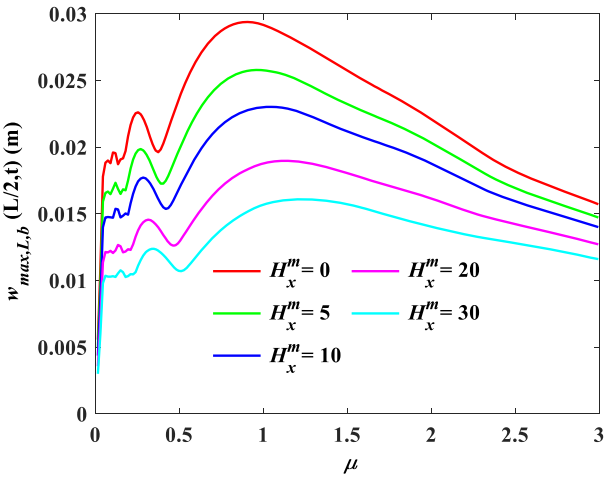

Fig. 11. Velocity dependant change of the maximum displacement of the midpoint of bridge beam for various dimensionless magnetic field intensity H_x^m=0, 5, 10, 20, 30, where the analysis results of the full train model with track at speed parameter μ between 0 and 3, and five different magnetic field intensities and when it passes over a 50 m long bridge are given in colour graphics. Here, the graph H_x^m=0 is represented in red, the graph H_x^m=5 in green, the graph H_x^m=10 in blue, the graph H_x^m=20 in magenta, and the graph H_x^m=30 in cyan.

direction is reduced by almost 50%.

The train's speed determines the train's excitation frequency on the bridge. When this excitation frequency equals the beam's vibration frequency, the train reaches a critical speed. At this speed, the bridge starts to vibrate at maximum amplitude. Vibration amplitudes are maximum when the train speed is at the excitation frequency of the train-bridge system. In this context, when Fig. 5 is examined, it is seen that the vertical acceleration of the train body is quite high if the train speed is at critical velocities. For example, in Fig. 5a, since the speed of the train is far from the second critical speed, the vibration amplitudes can be reduced by 60% thanks to the magnetic field, while in Fig. 5d, when the train speed is taken the same as the second critical speed, even in the case of the magnetic field, the vertical acceleration values are only %29 was reduced. In addition, another detail in Fig. 5b is that when the train speed is $0.25v_{cr}$, the vertical acceleration of the train body decreases by about 8%. The reason for this decrease is that it is remarkably close to the first critical speed of the train-bridge system.

However, the critical speeds of the train-bridge system are not constant due to the magnetic field effect. As the magnetic field intensity increases, the maximum amplitudes decrease significantly, and the velocity parameter at which it occurs increases. If the magnetic field intensity is zero, the maximum displacement of the bridge midpoint at critical speeds is more than the static displacement, that is, DAF exceeds 1, half thanks reduce the DAF of the midpoint of the bridge to the magnetic field.

The train-track-bridge interaction can be analyzed in detail using the proposed method. In addition, the magnetic field intensity can be used to control the system's dynamic behavior. In other words, the vibration responses of the train can be controlled by keeping the rigidity of the railway bridge at the desired level.

CRediT authorship contribution statement

Mustafa Eroğlu: Methodology, Software, Validation, Investigation, Writing – original draft, Visualization. **Mehmet Akif Koç:** Conceptualization, Software, Writing – review & editing, Visualization. **İsmail Esen:** Methodology, Writing – review & editing, Supervision.

Declaration of Competing Interest

The authors declare that they have no known competing financial interests or personal relationships that could have appeared to influence the work reported in this paper.

The authors declare the following financial interests/personal relationships which may be considered as potential competing interests:

Data availability

Data will be made available on request.

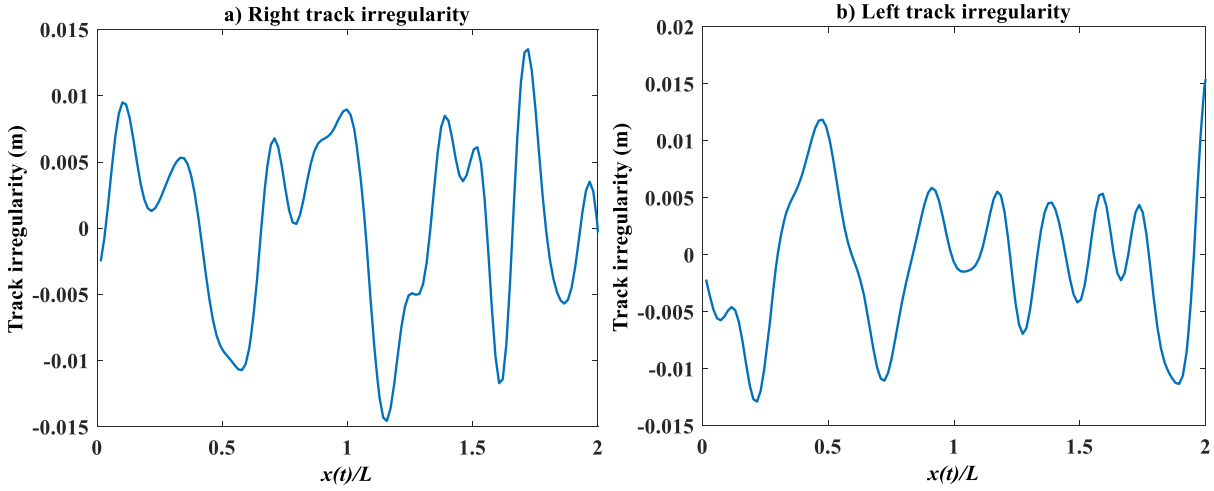

Fig. 12. Random track irregularity (a) Right track irregularity (b) Left track irregularity, where the horizontal axis shows the train's position relative to the bridge. When $x(t)/L$=1, the train has left the bridge.

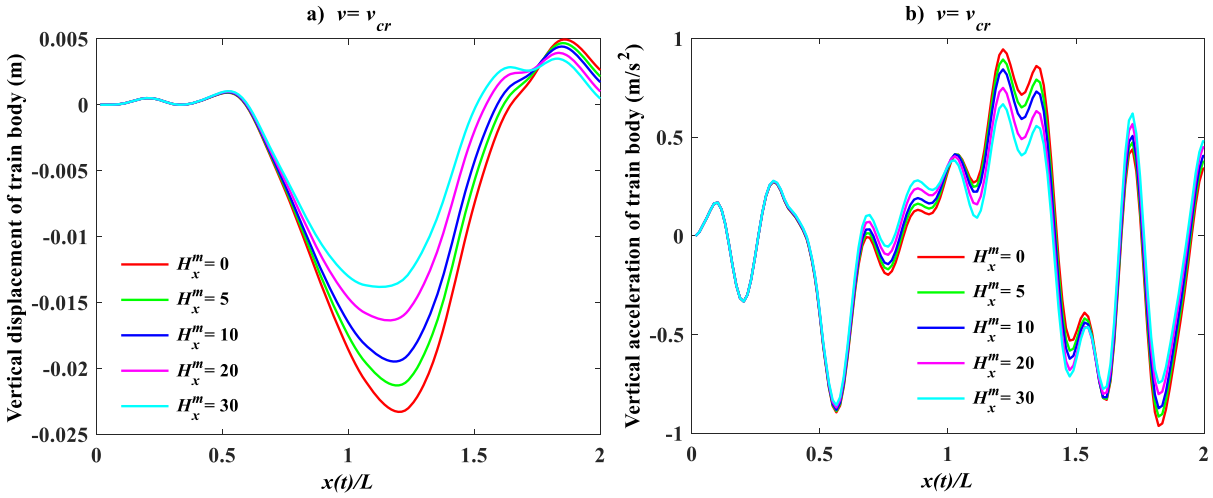

Fig. 13. Time dependant response of the vertical displacement and acceleration of train body for various dimensionless magnetic field intensity and random track irregularity H_x^m=0, 5, 10, 20, 30. (a) v=v_{cr} and vertical displacement of train body (b) v=v_{cr} and vertical acceleration of train body; for dimensionless time $x(t)/L$, L=50 m, where the analysis results of the full train model with the track at four different speeds and five different dimensionless magnetic field intensities are given in colour graphics. Here, the graph H_x^m=0 is represented in red, the graph H_x^m=5 in green, the graph H_x^m=10 in blue, the graph H_x^m=20 in magenta, and the graph H_x^m=30 in cyan.

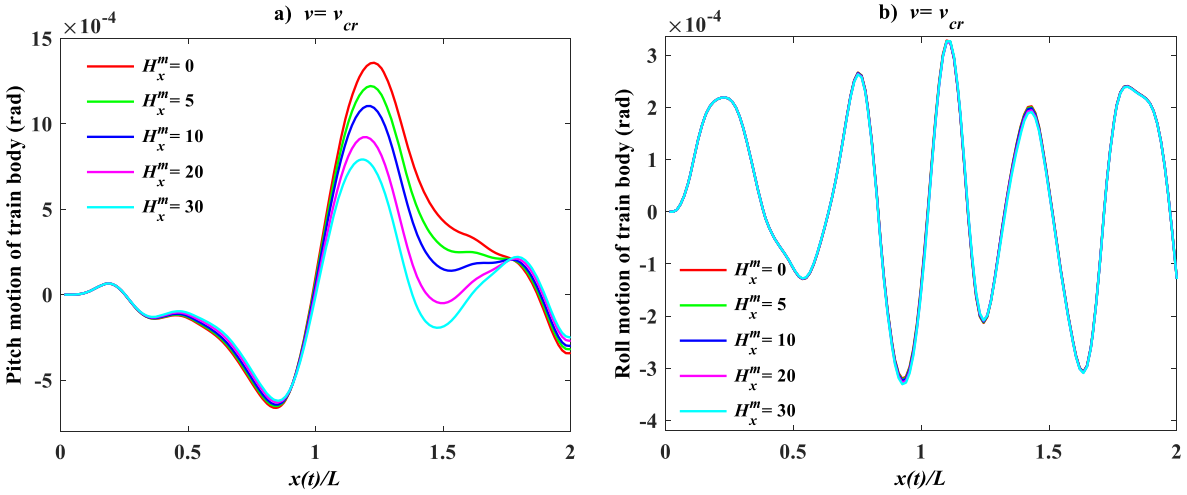

Fig. 14. Time dependant response of the pitch and roll motion of train body for various dimensionless magnetic field intensity and random track irregularity H_x^m=0, 5, 10, 20, 30. (a) v=v_{cr} and vertical displacement of train body (b) v=v_{cr} and vertical acceleration of train body; for dimensionless time $x(t)/L$, L=50 m, where the analysis results of the full train model with the track at four different speeds and five different dimensionless magnetic field intensities are given in colour graphics. Here, the graph H_x^m=0 is represented in red, the graph H_x^m=5 in green, the graph H_x^m=10 in blue, the graph H_x^m=20 in magenta, and the graph H_x^m=30 in cyan.

Appendix A

In Appendix (A.1-A.3), the kinetic energy, potential energy, and Rayleigh damping function of the TTBi system are given. In this study, the symbol R in the parameter indices represents the right, while the symbol L represents the left. For example, the parameters $\mu_{R,r}$, $\mu_{R,b}$, $\mu_{L,r}$, and $\mu_{L,b}$ represent the mass per unit length of the right rail, right bridge, left rail and left bridge, respectively. Similarly, the parameters $w_{R,r}$, $w_{R,b}$, $w_{L,r}$, and $w_{L,b}$ represent the vertical displacement of the right rail, right bridge, left rail and left the bridge at a given time t. The flexural stiffness of the right and left rail beams and bridge beams are represented by the values $E_{R,r}I_{R,r}$, $E_{L,r}I_{L,r}$, $E_{R,b}I_{R,b}$, and $E_{L,b}I_{L,b}$. On the other hand, (A.3) may be used to determine the dissipation function of the complete railway car model and the associated flexible structure system. The right and left Euler-Bernoulli rail beam and bridge beam's corresponding viscous damping coefficients are represented by the parameters $c_{R,r}$, $c_{L,r}$, $c_{R,b}$, and $c_{L,b}$ given in (A.3).

$$E_k = \frac{1}{2}\left[\begin{array}{l}\int_0^L \mu_{R,r}\left[\dot{w}^2_{R,r}(x,t)\right]dx + \int_0^L \mu_{R,b}\left[\dot{w}^2_{R,b}(x,t)\right]dx + \int_0^L \mu_{L,r}\left[\dot{w}^2_{L,r}(x,t)\right]dx + \int_0^L \mu_{L,b}\left[\dot{w}^2_{L,b}(x,t)\right]dx \\ +m_c\dot{r}^2_{cy} + m_c\dot{r}^2_{cz} + I_{cz}\dot{\theta}^2_{cz} + I_{cx}\dot{\theta}^2_{cx} + m_{b1}\dot{r}^2_{b1y} + m_{b1}\dot{r}^2_{b1z} + I_{b1z}\dot{\theta}^2_{b1z} + I_{b1x}\dot{\theta}^2_{b1x} + m_{b2}\dot{r}^2_{b2y} + m_{b2}\dot{r}^2_{b2z} \\ +I_{b2z}\dot{\theta}^2_{b2z} + I_{b2x}\dot{\theta}^2_{b2x} + m_w\dot{r}^2_{w1y} + m_w\dot{r}^2_{w1z} + I_{w1x}\dot{\theta}^2_{w1x} + m_w\dot{r}^2_{w2y} + m_w\dot{r}^2_{w2z} + I_{w2x}\dot{\theta}^2_{w2x} + m_w\dot{r}^2_{w3y} \\ +m_w\dot{r}^2_{w3z} + I_{w3x}\dot{\theta}^2_{w3x} + m_w\dot{r}^2_{w4y} + m_w\dot{r}^2_{w4z} + I_{w4x}\dot{\theta}^2_{w4x} + m_{R,s}\dot{w}^2_{R,s} + m_{R,ba}\dot{w}^2_{R,ba} + m_{L,s}\dot{w}^2_{L,s} + m_{L,ba}\dot{w}^2_{L,ba}\end{array}\right] \tag{A.1}$$

$$E_p = \frac{1}{2}\left[\begin{array}{l}\int_0^L E_{R,r}I_{R,r}\left[w''^2_{R,r}(x,t)\right]dx + \int_0^L E_{R,b}I_{R,b}\left[w''^2_{R,b}(x,t)\right]dx + \int_0^L E_{L,r}I_{L,r}\left[w''^2_{L,r}(x,t)\right]dx + \int_0^L E_{L,b}I_{L,b}\left[w''^2_{L,b}(x,t)\right]dx \\ +k_{b1y}\left[r_{cy} - r_{b1y} + \theta_{cz}l_{b1} - \theta_{cx}a + \theta_{b1x}a\right]^2 + k_{b1y}\left[r_{cy} - r_{b1y} + \theta_{cz}l_{b1} + \theta_{cx}a - \theta_{b1x}a\right]^2 \\ +k_{b2y}\left[r_{cy} - r_{b2y} - \theta_{cz}l_{b2} - \theta_{cx}a + \theta_{b2x}a\right]^2 + k_{b2y}\left[r_{cy} - r_{b2y} - \theta_{cz}l_{b2} + \theta_{cx}a - \theta_{b2x}a\right]^2 \\ +k_{w1y}\left[r_{b1y} - r_{w1y} + \theta_{b1z}l_{w1} - \theta_{b1x}d + \theta_{w1x}d\right]^2 + k_{w1y}\left[r_{b1y} - r_{w1y} + \theta_{b1z}l_{w1} + \theta_{b1x}d - \theta_{w1x}d\right]^2 \\ +k_{w2y}\left[r_{b1y} - r_{w2y} - \theta_{b1z}l_{w2} - \theta_{b1x}d + \theta_{w2x}d\right]^2 + k_{w2y}\left[r_{b1y} - r_{w2y} - \theta_{b1z}l_{w2} + \theta_{b1x}d - \theta_{w2x}d\right]^2 \\ +k_{w3y}\left[r_{b2y} - r_{w3y} + \theta_{b2z}l_{w3} - \theta_{b2x}d + \theta_{w3x}d\right]^2 + k_{w3y}\left[r_{b2y} - r_{w3y} + \theta_{b2z}l_{w3} + \theta_{b2x}d - \theta_{w3x}d\right]^2 \\ +k_{w4y}\left[r_{b2y} - r_{w4y} - \theta_{b2z}l_{w4} - \theta_{b2x}d + \theta_{w4x}d\right]^2 + k_{w4y}\left[r_{b2y} - r_{w4y} - \theta_{b2z}l_{w4} + \theta_{b2x}d - \theta_{w4x}d\right]^2 \\ +2k_{bz}[r_{cz} - r_{b1z} - \theta_{cx}h_c - \theta_{b1x}h_b]^2 + 2k_{bz}[r_{cz} - r_{b2z} - \theta_{cx}h_c - \theta_{b2x}h_b]^2 + 2k_{wz}[r_{b1z} - r_{w1z} - \theta_{b1x}h_w]^2 \\ +2k_{wz}[r_{b1z} - r_{w2z} - \theta_{b1x}h_w]^2 + 2k_{wz}[r_{b2z} - r_{w3z} - \theta_{b2x}h_w]^2 + 2k_{wz}[r_{b2z} - r_{w4z} - \theta_{b2x}h_w]^2 + k_p\left[w_{r,l} - w_{s,l}\right]^2 \\ +k_p\left[w_{r,r} - w_{s,r}\right]^2 + k_b\left[w_{s,l} - w_{ba,l}\right]^2 + k_b\left[w_{s,r} - w_{ba,r}\right]^2 + k_f\left[w_{ba,l} - w_{b,l}\right]^2 + k_f\left[w_{ba,r} - w_{b,r}\right]^2\end{array}\right] \tag{A.2}$$

$$D = \frac{1}{2}\left[\begin{array}{l}\int_0^L c_{R,r}\dot{w}^2_{R,r}(x,t)dx + \int_0^L c_{R,b}\dot{w}^2_{R,b}(x,t)dx + \int_0^L c_{L,r}\dot{w}^2_{L,r}(x,t)dx + \int_0^L c_{L,b}\dot{w}^2_{L,b}(x,t)dx \\ +c_{b1y}\left[\dot{r}_{cy} - \dot{r}_{b1y} + \dot{\theta}_{cz}l_{b1} - \dot{\theta}_{cx}a + \dot{\theta}_{b1x}a\right]^2 + c_{b1y}\left[\dot{r}_{cy} - \dot{r}_{b1y} + \dot{\theta}_{cz}l_{b1} + \dot{\theta}_{cx}a - \dot{\theta}_{b1x}a\right]^2 \\ +c_{b2y}\left[\dot{r}_{cy} - \dot{r}_{b2y} - \dot{\theta}_{cz}l_{b2} - \dot{\theta}_{cx}a + \dot{\theta}_{b2x}a\right]^2 + c_{b2y}\left[\dot{r}_{cy} - \dot{r}_{b2y} - \dot{\theta}_{cz}l_{b2} + \dot{\theta}_{cx}a - \dot{\theta}_{b2x}a\right]^2 \\ +c_{w1y}\left[\dot{r}_{b1y} - \dot{r}_{w1y} + \dot{\theta}_{b1z}l_{w1} - \dot{\theta}_{b1x}d + \dot{\theta}_{w1x}d\right]^2 + c_{w1y}\left[\dot{r}_{b1y} - \dot{r}_{w1y} + \dot{\theta}_{b1z}l_{w1} + \dot{\theta}_{b1x}d - \dot{\theta}_{w1x}d\right]^2 \\ +c_{w2y}\left[\dot{r}_{b1y} - \dot{r}_{w2y} - \dot{\theta}_{b1z}l_{w2} - \dot{\theta}_{b1x}d + \dot{\theta}_{w2x}d\right]^2 + c_{w2y}\left[\dot{r}_{b1y} - \dot{r}_{w2y} - \dot{\theta}_{b1z}l_{w2} + \dot{\theta}_{b1x}d - \dot{\theta}_{w2x}d\right]^2 \\ +c_{w3y}\left[\dot{r}_{b2y} - \dot{r}_{w3y} + \dot{\theta}_{b2z}l_{w3} - \dot{\theta}_{b2x}d + \dot{\theta}_{w3x}d\right]^2 + c_{w3y}\left[\dot{r}_{b2y} - \dot{r}_{w3y} + \dot{\theta}_{b2z}l_{w3} + \dot{\theta}_{b2x}d - \dot{\theta}_{w3x}d\right]^2 \\ +c_{w4y}\left[\dot{r}_{b2y} - \dot{r}_{w4y} - \dot{\theta}_{b2z}l_{w4} - \dot{\theta}_{b2x}d + \dot{\theta}_{w4x}d\right]^2 + c_{w4y}\left[\dot{r}_{b2y} - \dot{r}_{w4y} - \dot{\theta}_{b2z}l_{w4} + \dot{\theta}_{b2x}d - \dot{\theta}_{w4x}d\right]^2 \\ +2c_{bz}[\dot{r}_{cz} - \dot{r}_{b1z} - \dot{\theta}_{cx}h_c - \dot{\theta}_{b1x}h_b]^2 + 2c_{bz}[\dot{r}_{cz} - \dot{r}_{b2z} - \dot{\theta}_{cx}h_c - \dot{\theta}_{b2x}h_b]^2 + 2c_{wz}[\dot{r}_{b1z} - \dot{r}_{w1z} - \dot{\theta}_{b1x}h_w]^2 \\ +2c_{wz}[\dot{r}_{b1z} - \dot{r}_{w2z} - \dot{\theta}_{b1x}h_w]^2 + 2c_{wz}[\dot{r}_{b2z} - \dot{r}_{w3z} - \dot{\theta}_{b2x}h_w]^2 + 2c_{wz}[\dot{r}_{b2z} - \dot{r}_{w4z} - \dot{\theta}_{b2x}h_w]^2 + c_p\left[\dot{w}_{r,l} - \dot{w}_{s,l}\right]^2 \\ +c_p\left[\dot{w}_{r,r} - \dot{w}_{s,r}\right]^2 + c_b\left[\dot{w}_{s,l} - \dot{w}_{ba,l}\right]^2 + c_b\left[\dot{w}_{s,r} - \dot{w}_{ba,r}\right]^2 + c_f\left[\dot{w}_{ba,l} - \dot{w}_{b,l}\right]^2 + c_f\left[\dot{w}_{ba,r} - \dot{w}_{b,r}\right]^2\end{array}\right] \tag{A.3}$$

The Lagrangian expression is the difference between the potential and kinetic energy provided in Eqs. (A.1) and (A.2), where $\boldsymbol{\phi_k}$ is the generalized coordinates of the train [80].

$$L = E_k - E_p \tag{A.4}$$

$$\frac{d}{dt}\left(\frac{\partial L}{\partial \dot{\phi}_k(t)}\right) - \frac{\partial L}{\partial \phi_k(t)} + \frac{\partial D}{\partial \dot{\phi}_k(t)} = 0,\ k = 1, 2, ..., 24, \tag{A.5}$$

Using (Eq. A.5), the motion equations of the train are determined.

Appendix B

Using the variables listed in Appendix B, second-order equations have been transformed into first-order equations.

$$
\begin{aligned}
&x_1 = r_{cy}\dot{x}_1 = \dot{r}_{cy} = x_2x_{16} = \dot{\theta}_{b1x}\dot{x}_{16} = \ddot{\theta}_{b1x}x_{31} = r_{w2y}\dot{x}_{31} = \dot{r}_{w2y} = x_{32}x_{46} = \dot{r}_{w4z}\dot{x}_{46} = \ddot{r}_{w4z}\\
&x_2 = \dot{r}_{cy}\dot{x}_2 = \ddot{r}_{cy}x_{17} = r_{b2y}\dot{x}_{17} = \dot{r}_{b2y} = x_{18}x_{32} = \dot{r}_{w2y}\dot{x}_{32} = \ddot{r}_{w2y}x_{47} = \theta_{w4x}\dot{x}_{47} = \dot{\theta}_{w4x} = x_{48}\\
&x_3 = r_{cz}\dot{x}_3 = \dot{r}_{cz} = x_4x_{18} = \dot{r}_{b2y}\dot{x}_{18} = \ddot{r}_{b2y}x_{33} = r_{w2z}\dot{x}_{33} = \dot{r}_{w2z} = x_{34}x_{48} = \dot{\theta}_{w4x}\dot{x}_{48} = \ddot{\theta}_{w4x}\\
&x_4 = \dot{r}_{cz}\dot{x}_4 = \ddot{r}_{cz}x_{19} = r_{b2z}\dot{x}_{19} = \dot{r}_{b2z} = x_{20}x_{34} = \dot{r}_{w2z}\dot{x}_{34} = \ddot{r}_{w2z}x_{49} = q_1\dot{x}_{49} = \dot{q}_1 = x_{50}\\
&x_5 = \theta_{cz}\dot{x}_5 = \dot{\theta}_{cz} = x_6x_{20} = \dot{r}_{b2z}\dot{x}_{20} = \ddot{r}_{b2z}x_{35} = \theta_{w2x}\dot{x}_{35} = \dot{\theta}_{w2x} = x_{36}\vdots\\
&x_6 = \dot{\theta}_{cz}\dot{x}_6 = \ddot{\theta}_{cz}x_{21} = \theta_{b2z}\dot{x}_{21} = \dot{\theta}_{b2z} = x_{22}x_{36} = \dot{\theta}_{w2x}\dot{x}_{36} = \ddot{\theta}_{w2x}x_{48+4n} = \dot{q}_n\dot{x}_{48+4n} = \ddot{q}_n\\
&x_7 = \theta_{cx}\dot{x}_7 = \dot{\theta}_{cx} = x_8x_{22} = \dot{\theta}_{b2z}\dot{x}_{22} = \ddot{\theta}_{b2z}x_{37} = r_{w3y}\dot{x}_{37} = \dot{r}_{w3y} = x_{38}x_{48+4n+1} = \gamma_1\dot{x}_{48+4n+1} = \dot{\gamma}_1\\
&x_8 = \dot{\theta}_{cx}\dot{x}_8 = \ddot{\theta}_{cx}x_{23} = \theta_{b2x}\dot{x}_{23} = \dot{\theta}_{b2x} = x_{24}x_{38} = \dot{r}_{w3y}\dot{x}_{38} = \ddot{r}_{w3y}\vdots\\
&x_9 = r_{b1y}\dot{x}_9 = \dot{r}_{b1y} = x_{10}x_{24} = \dot{\theta}_{b2x}\dot{x}_{24} = \ddot{\theta}_{b2x}x_{39} = r_{w3z}\dot{x}_{39} = \dot{r}_{w3z} = x_{40}x_{48+8n} = \dot{\gamma}_n\dot{x}_{48+8n} = \ddot{\gamma}_n\\
&x_{10} = \dot{r}_{b1y}\dot{x}_{10} = \ddot{r}_{b1y}x_{25} = r_{w1y}\dot{x}_{25} = \dot{r}_{w1y} = x_{26}x_{40} = \dot{r}_{w3z}\dot{x}_{40} = \ddot{r}_{w3z}x_{48+8n+1} = \psi_1\dot{x}_{48+8n+1} = \dot{\psi}\\
&x_{11} = r_{b1z}\dot{x}_{11} = \dot{r}_{b1z} = x_{12}x_{26} = \dot{r}_{w1y}\dot{x}_{26} = \ddot{r}_{w1y}x_{41} = \theta_{w3x}\dot{x}_{41} = \dot{\theta}_{w3x} = x_{42}\vdots\\
&x_{12} = \dot{r}_{b1z}\dot{x}_{12} = \ddot{r}_{b1z}x_{27} = r_{w1z}\dot{x}_{27} = \dot{r}_{w1z} = x_{28}x_{42} = \dot{\theta}_{w3x}\dot{x}_{42} = \ddot{\theta}_{w3x}x_{48+12n} = \dot{\psi}_n\dot{x}_{48+12n} = \ddot{\psi}_n\\
&x_{13} = \theta_{b1z}\dot{x}_{13} = \dot{\theta}_{b1z} = x_{14}x_{28} = \dot{r}_{w1z}\dot{x}_{28} = \ddot{r}_{w1z}x_{43} = r_{w4y}\dot{x}_{43} = \dot{r}_{w4y} = x_{44}\vdots\\
&x_{14} = \dot{\theta}_{b1z}\dot{x}_{14} = \ddot{\theta}_{b1z}x_{29} = \theta_{w1x}\dot{x}_{29} = \dot{\theta}_{w1x} = x_{30}x_{44} = \dot{r}_{w4y}\dot{x}_{44} = \ddot{r}_{w4y}x_{48+12n+1} = \phi_1\dot{x}_{48+12n+1} = \dot{\phi}\\
&x_{15} = \theta_{b1x}\dot{x}_{15} = \dot{\theta}_{b1x} = x_{16}x_{30} = \dot{\theta}_{w1x}\dot{x}_{30} = \ddot{\theta}_{w1x}x_{45} = r_{w4z}\dot{x}_{45} = \dot{r}_{w4z} = x_{46}x_{48+16n} = \dot{\phi}_n\dot{x}_{48+16n} = \ddot{\phi}
\end{aligned}
\tag{B.1}
$$

The following results are obtained when equations are written in a state-space form using state variables provided by Eq. (B.1) together with equation movements corresponding to other coordinates.

$$\dot{\mathbf{X}}(t) = A(t)\mathbf{X}(t) + f(t), \tag{B.2}$$

$$\mathbf{X}(t) = \{x_1x_2...x_{48+(16n-1)}x_{48+16n}\}^T, \tag{B.3}$$

For the differential equation system, which consists of a total of sixty-two first-order differential equations, four repeating coefficients of the Runge-Kutta technique are stated as follows.

$$
\begin{aligned}
&k^i_{1(1)} = f\left(t_i, x_{1(i)}, x_{2(i)}, x_{3(i)}, ..., x_{48+16n(i)}\right),\\
&\vdots\\
&k^i_{1(48+16n)} = f\left(t_i, x_{1(i)}, x_{2(i)}, x_{3(i)}, ..., x_{48+16n(i)}\right),
\end{aligned}
\tag{B.4}
$$

$$
\begin{aligned}
&k^i_{2(1)} = f\left(t_i + \frac{1}{2}\Delta t, x_{1(i)} + \frac{1}{2}k^i_{1(1)}\Delta t, x_{2(i)} + \frac{1}{2}k^i_{1(2)}\Delta t, x_{3(i)} + \frac{1}{2}k^i_{1(3)}\Delta t, ..., x_{48+16n(i)} + \frac{1}{2}k^i_{1(48+16n)}\Delta t\right),\\
&\vdots\\
&k^i_{2(48+16n)} = f\left(t_i + \frac{1}{2}\Delta t, x_{1(i)} + \frac{1}{2}k^i_{1(1)}\Delta t, x_{2(i)} + \frac{1}{2}k^i_{1(2)}\Delta t, x_{3(i)} + \frac{1}{2}k^i_{1(3)}\Delta t, .., x_{48+16n(i)} + \frac{1}{2}k^i_{1(48+16n)}\Delta t\right),
\end{aligned}
\tag{B.5}
$$

$$
\begin{aligned}
&k^i_{3(1)} = f\left(t_i + \frac{1}{2}\Delta t, x_{1(i)} + \frac{1}{2}k^i_{2(1)}\Delta t, x_{2(i)} + \frac{1}{2}k^i_{2(2)}\Delta t, x_{3(i)} + \frac{1}{2}k^i_{2(3)}\Delta t, ..., x_{48+16n(i)} + \frac{1}{2}k^i_{2(48+16n(i))}\Delta t\right),\\
&\vdots\\
&k^i_{3(48+16n)} = f\left(t_i + \frac{1}{2}\Delta t, x_{1(i)} + \frac{1}{2}k^i_{2(1)}\Delta t, x_{2(i)} + \frac{1}{2}k^i_{2(2)}\Delta t, x_{3(i)} + \frac{1}{2}k^i_{2(3)}\Delta t, ..., x_{48+16n(i)} + \frac{1}{2}k^i_{2(48+16n)}\Delta t\right),
\end{aligned}
\tag{B.6}
$$

$$
\begin{aligned}
&k^i_{4(1)} = f\left(t_i + \Delta t, x_{1(i)} + k^i_{3(1)}\Delta t, x_{2(i)} + k^i_{3(2)}\Delta t, x_{3(i)} + k^i_{3(3)}\Delta t, ..., x_{48+16n(i)} + k^i_{3(48+16n)}\Delta t\right),\\
&\vdots\\
&k^i_{4(48+16n)} = f\left(t_i + \Delta t, x_{1(i)} + k^i_{3(1)}\Delta t, x_{2(i)} + k^i_{3(2)}\Delta t, x_{3(i)} + k^i_{3(3)}\Delta t, ..., x_{48+16n(i)} + k^i_{3(48+16n)}\Delta t\right),
\end{aligned}
\tag{B.7}
$$

$$
\begin{aligned}
&x_{1(i+1)} = x_{1(i)} + \frac{\Delta t}{6}\left(k^i_{1(1)} + 2k^i_{2(1)} + 2k^i_{3(1)} + k^i_{4(1)}\right)\\
&x_{2(i+1)} = x_{2(i)} + \frac{\Delta t}{6}\left(k^i_{1(2)} + 2k^i_{2(2)} + 2k^i_{3(2)} + k^i_{4(2)}\right)\\
&\vdots\\
&x_{(48+16n)(i+1)} = x_{(48+16n)(i)} + \frac{\Delta t}{6}\left(k^i_{1(48+16n)} + 2k^i_{2(48+16n)} + 2k^i_{3(48+16n)} + k^i_{4(48+16n)}\right)
\end{aligned}
\tag{B.8}
$$

Appendix C

By using Appendix A, the motion equations of the train are determined as follows. The following are the methods for obtaining the car's body's motion equations:

$$\ddot{r}_{cy} = \frac{1}{m_c}\begin{bmatrix} -2c_{b1y}\left[\dot{r}_{cy} - \dot{r}_{b1y} + \dot{\theta}_{cz}l_{b1}\right] - 2c_{b2y}\left[\dot{r}_{cy} - \dot{r}_{b2y} - \dot{\theta}_{cz}l_{b2}\right] \\ -2k_{b1y}\left[r_{cy} - r_{b1y} + \theta_{cz}l_{b1}\right] - 2k_{b2y}\left[r_{cy} - r_{b2y} - \theta_{cz}l_{b2}\right] \end{bmatrix} \tag{C.1}$$

$$\ddot{r}_{cz} = \frac{1}{m_c}\begin{bmatrix} -2c_{bz}[2\dot{r}_{cz} - \dot{r}_{b1z} - \dot{r}_{b2z} - 2\dot{\theta}_{cx}h_c - \dot{\theta}_{b1x}h_b - \dot{\theta}_{b2x}h_b] \\ -2k_{bz}[2r_{cz} - r_{b1z} - r_{b2z} - 2\theta_{cx}h_c - \theta_{b1x}h_b - \theta_{b2x}h_b] \end{bmatrix} \tag{C.2}$$

$$\ddot{\theta}_{cz}=\frac{1}{I_{cz}}\begin{bmatrix}-2c_{b1y}l_{b1}\left[\dot{r}_{cy}-\dot{r}_{b1y}+\dot{\theta}_{cz}l_{b1}\right]+2c_{b2y}l_{b2}\left[\dot{r}_{cy}-\dot{r}_{b2y}-\dot{\theta}_{cz}l_{b2}\right]\\-2k_{b1y}l_{b1}\left[r_{cy}-r_{b1y}+\theta_{cz}l_{b1}\right]+2k_{b2y}l_{b2}\left[r_{cy}-r_{b2y}-\theta_{cz}l_{b2}\right]\end{bmatrix} \tag{C.3}$$

$$\ddot{\theta}_{cx}=\frac{1}{I_{cx}}\begin{bmatrix}-2c_{b1y}a^2\left[\dot{\theta}_{cx}-\dot{\theta}_{b1x}\right]-2c_{b2y}a^2\left[\dot{\theta}_{cx}-\dot{\theta}_{b2x}\right]\\-2k_{b1y}a^2\left[\theta_{cx}-\theta_{b1x}\right]-2k_{b2y}a^2\left[\theta_{cx}-\theta_{b2x}\right]\end{bmatrix} \tag{C.4}$$

The equations of motion of the front bogie have been written as Eq. (7f-1):

$$\ddot{r}_{b1y}=\frac{1}{m_{b1}}\begin{bmatrix}2c_{b1y}\left[\dot{r}_{cy}-\dot{r}_{b1y}+\dot{\theta}_{cz}l_{b1}\right]-c_{w1y}\left[2\dot{r}_{b1y}-\varphi_i(\xi_{1R},t)\dot{q}_i-\varphi_i(\xi_{1L},t)\dot{q}_i+2\dot{\theta}_{b1z}l_{w1}\right]\\-c_{w2y}\left[2\dot{r}_{b1y}-\varphi_i(\xi_{2R},t)\dot{q}_i-\varphi_i(\xi_{2L},t)\dot{q}_i-2\dot{\theta}_{b1z}l_{w2}\right]+2k_{b1y}\left[r_{cy}-r_{b1y}+\theta_{cz}l_{b1}\right]\\-k_{w1y}\left[2r_{b1y}-\varphi_i(\xi_{1R},t)q_i-\varphi_i(\xi_{1L},t)q_i+2\theta_{b1z}l_{w1}\right]\\-k_{w2y}\left[2r_{b1y}-\varphi_i(\xi_{2R},t)q_i-\varphi_i(\xi_{2L},t)q_i-2\theta_{b1z}l_{w2}\right]\end{bmatrix} \tag{C.5}$$

$$\ddot{r}_{b1z}=\frac{1}{m_{b1}}\begin{bmatrix}2c_{bz}\left[\dot{r}_{cz}-\dot{r}_{b1z}-\dot{\theta}_{cx}h_c+\dot{\theta}_{b1x}h_b\right]-2c_{wz}\left[2\dot{r}_{b1z}-\dot{r}_{w1z}-\dot{r}_{w2z}-2\dot{\theta}_{b1x}h_w\right]\\+2k_{bz}\left[r_{cz}-r_{b1z}-\theta_{cx}h_c+\theta_{b1x}h_b\right]-2k_{wz}\left[2r_{b1z}-r_{w1z}-r_{w2z}-2\theta_{b1x}h_w\right]\end{bmatrix} \tag{C.6}$$

$$\ddot{\theta}_{b1z}=\frac{1}{I_{b1z}}\begin{bmatrix}c_{w2y}l_{w2}\left[2\dot{r}_{b1y}-\varphi_i(\xi_{2R},t)\dot{q}_i-\varphi_i(\xi_{2L},t)\dot{q}_i-2\dot{\theta}_{b1z}l_{w2}\right]\\-c_{w1y}l_{w1}\left[2\dot{r}_{b1y}-\varphi_i(\xi_{1R},t)\dot{q}_i-\varphi_i(\xi_{1L},t)\dot{q}_i+2\dot{\theta}_{b1z}l_{w1}\right]\\-k_{w1y}l_{w1}\left[2r_{b1y}-\varphi_i(\xi_{1R},t)q_i-\varphi_i(\xi_{1L},t)q_i+2\theta_{b1z}l_{w1}\right]\\+k_{w2y}l_{w2}\left[2r_{b1y}-\varphi_i(\xi_{2R},t)q_i-\varphi_i(\xi_{2L},t)q_i-2\theta_{b1z}l_{w2}\right]\end{bmatrix} \tag{C.7}$$

$$\ddot{\theta}_{b1x}=\frac{1}{I_{b1x}}\begin{bmatrix}2c_{b1y}a^2\left[\dot{\theta}_{cx}-\dot{\theta}_{b1x}\right]+c_{w1y}d\left[2\dot{\theta}_{w1x}d-\varphi_i(\xi_{1R},t)\dot{q}_i+\varphi_i(\xi_{1L},t)\dot{q}_i-2\dot{\theta}_{b1x}d\right]\\+c_{w2y}d\left[2\dot{\theta}_{w2x}d-\varphi_i(\xi_{2R},t)\dot{q}_i+\varphi_i(\xi_{2L},t)\dot{q}_i-2\dot{\theta}_{b1x}d\right]+2k_{b1y}a^2\left[\theta_{cx}-\theta_{b1x}\right]\\+k_{w1y}d\left[2\theta_{w1x}d-\varphi_i(\xi_{1R},t)q_i+\varphi_i(\xi_{1L},t)q_i-2\theta_{b1x}d\right]\\+k_{w2y}d\left[2\theta_{w2x}d-\varphi_i(\xi_{2R},t)q_i+\varphi_i(\xi_{2L},t)q_i-2\theta_{b1x}d\right]\end{bmatrix} \tag{C.8}$$

The equations of motion of the rear bogie are given as follows:

$$\ddot{r}_{b2y}=\frac{1}{m_{b2}}\begin{bmatrix}2c_{b2y}\left[\dot{r}_{cy}-\dot{r}_{b2y}-\dot{\theta}_{cz}l_{b2}\right]-c_{w3y}\left[2\dot{r}_{b2y}-\varphi_i(\xi_{3R},t)\dot{q}_i-\varphi_i(\xi_{3L},t)\dot{q}_i+2\dot{\theta}_{b2z}l_{w3}\right]\\-c_{w4y}\left[2\dot{r}_{b2y}-\varphi_i(\xi_{4R},t)\dot{q}_i-\varphi_i(\xi_{4L},t)\dot{q}_i-2\dot{\theta}_{b2z}l_{w4}\right]+2k_{b2y}\left[r_{cy}-r_{b2y}-\theta_{cz}l_{b2}\right]\\-k_{w3y}\left[2r_{b2y}-\varphi_i(\xi_{3R},t)q_i-\varphi_i(\xi_{3L},t)q_i+2\theta_{b2z}l_{w3}\right]\\-k_{w4y}\left[2r_{b2y}-\varphi_i(\xi_{4R},t)q_i-\varphi_i(\xi_{4L},t)q_i-2\theta_{b2z}l_{w4}\right]\end{bmatrix} \tag{C.9}$$

$$\ddot{r}_{b2z}=\frac{1}{m_{b2}}\begin{bmatrix}2c_{bz}\left[\dot{r}_{cz}-\dot{r}_{b2z}-\dot{\theta}_{cx}h_c-\dot{\theta}_{b2x}h_b\right]-2c_{wz}\left[2\dot{r}_{b2z}-\dot{r}_{w3z}-\dot{r}_{w4z}-2\dot{\theta}_{b2x}h_w\right]\\+2k_{bz}\left[r_{cz}-r_{b2z}-\theta_{cx}h_c-\theta_{b2x}h_b\right]-2k_{wz}\left[2r_{b2z}-r_{w3z}-r_{w4z}-2\theta_{b2x}h_w\right]\end{bmatrix} \tag{C.10}$$

$$\ddot{\theta}_{b2z}=\frac{1}{I_{b2z}}\begin{bmatrix}c_{w4y}l_{w4}\left[2\dot{r}_{b2y}-\varphi_i(\xi_{4R},t)\dot{q}_i-\varphi_i(\xi_{4L},t)\dot{q}_i-2\dot{\theta}_{b2z}l_{w4}\right]\\-c_{w3y}l_{w3}\left[2\dot{r}_{b2y}-\varphi_i(\xi_{3R},t)\dot{q}_i-\varphi_i(\xi_{3L},t)\dot{q}_i+2\dot{\theta}_{b2z}l_{w3}\right]\\k_{w4y}l_{w4}\left[2r_{b2y}-\varphi_i(\xi_{4R},t)q_i-\varphi_i(\xi_{4L},t)q_i-2\theta_{b2z}l_{w4}\right]\\-k_{w3y}l_{w3}\left[2r_{b2y}-\varphi_i(\xi_{3R},t)q_i-\varphi_i(\xi_{3L},t)q_i+2\theta_{b2z}l_{w3}\right]\end{bmatrix} \tag{C.11}$$

$$\ddot{\theta}_{b2x}=\frac{1}{I_{b2x}}\begin{bmatrix}2c_{b2y}a^2\left[\dot{\theta}_{cx}-\dot{\theta}_{b2x}\right]+c_{w3y}d\left[2\dot{\theta}_{w3x}d-\varphi_i(\xi_{3R},t)\dot{q}_i+\varphi_i(\xi_{3L},t)\dot{q}_i-2\dot{\theta}_{b2x}d\right]\\+c_{w4y}d\left[2\dot{\theta}_{w4x}d-\varphi_i(\xi_{4R},t)\dot{q}_i+\varphi_i(\xi_{4L},t)\dot{q}_i-2\dot{\theta}_{b2x}d\right]+2k_{b2y}a^2\left[\theta_{cx}-\theta_{b2x}\right]\\+k_{w3y}d\left[2\theta_{w3x}d-\varphi_i(\xi_{3R},t)q_i+\varphi_i(\xi_{3L},t)q_i-2\theta_{b2x}d\right]\\+k_{w4y}d\left[2\theta_{w4x}d-\varphi_i(\xi_{4R},t)q_i+\varphi_i(\xi_{4L},t)q_i-2\theta_{b2x}d\right]\end{bmatrix} \tag{C.12}$$

The equations of motion of wheelsets are given by Eqs. (C.13)–(15). (for k=1, 2 j=1 and for k=3, 4 j=2)
Vertical motion:

$$\ddot{r}_{wky}=\frac{1}{m_w}\left[2c_{wky}\left[\dot{r}_{bjy}-\dot{r}_{wky}+\dot{\theta}_{bjz}l_{wk}\right]+2k_{wky}\left[r_{bjy}-r_{wky}+\theta_{bjz}l_{wk}\right]\right] \tag{C.13}$$

Lateral motion:

$$\ddot{r}_{wkz}=\frac{1}{m_w}\left[2c_{wz}\left[\dot{r}_{bjz}-\dot{r}_{wkz}-\dot{\theta}_{bjx}h_w\right]+2k_{wz}\left[r_{bjz}-r_{wkz}-\theta_{bjx}h_w\right]\right] \tag{C.14}$$

Roll motion:

$$\ddot{\theta}_{wkx}=\frac{1}{I_{wkx}}\begin{bmatrix}c_{wky}d\left[2\dot{\theta}_{bjx}d-\varphi_i(\xi_{kL},t)\dot{q}_i+\varphi_i(\xi_{kR},t)\dot{q}_i-2\dot{\theta}_{wkx}d\right]\\+k_{wky}d\left[2\theta_{bjx}d-\varphi_i(\xi_{kL},t)q_i+\varphi_i(\xi_{kR},t)q_i-2\theta_{wkx}d\right]\end{bmatrix} \tag{C.15}$$

The 24 s-order differential equations of the 3D high-speed train are given above. In order to analyze the entire train-track-bridge coupled system, differential equations of the track and the bridge should be obtained. The Euler-Bernoulli beam theorem is used to simulate the rail and bridge in the track subsystem. The equations below give the 4th-degree motion equations of the rail and the bridge, respectively [81].

$$E_rI_r\frac{\partial^4w_r(x,t)}{\partial x^4}+\mu_r\frac{\partial^2w_r(x,t)}{\partial t^2}+2\mu_r\omega_r\frac{\partial w_r(x,t)}{\partial t}=-\sum_{i=1}^{n}\left[F_i\delta(x-x_i)-F_l\right] \tag{C.16}$$

$$E_b I_b \frac{\partial^4 w_b(x,t)}{\partial x^4} + \mu_b \frac{\partial^2 w_b(x,t)}{\partial t^2} + 2\mu_b \omega_b \frac{\partial w_b(x,t)}{\partial t} = -\sum_{i=1}^{n} \left[k_f(w_{ba} - w_b) + c_f(\dot{w}_{ba} - \dot{w}_b)\right]\delta(x - x_i) \tag{C.17}$$

$$x_1 = vt, x_2 = vt - 2l_w, x_3 = vt - l_{b1} - l_{b2}, x_4 = vt - l_{b1} - l_{b2} - 2l_w, \tag{C.18}$$

In the given equations, F represents the wheel force applied to the rail by the train, δ the Dirac-Delta function, ω_r, and ω_b represent the circular damping frequency of the rail and the bridge beam, respectively. x_i represents the position of the force acting on the rail and bridge relative to the left reference of the beam. The displacement of any x point on the beam at any time t is expressed using the Galerkin functions [82] $w_{R,r}(x,t)$, $w_{L,r}(x,t)$, $w_{R,b}(x,t)$, and $w_{L,b}(x,t)$, respectively.

$$\begin{aligned} w_{R,r}(x,t) &= \sum_{i=1}^{n} \varphi_i(x) q_i(t), \;\; w_{L,r}(x,t) = \sum_{i=1}^{n} \varphi_{i+n}(x) q_{i+n}(t), \\ w_{R,b}(x,t) &= \sum_{i=1}^{n} \varphi_i(x) \phi_i(t), \;\; w_{L,b}(x,t) = \sum_{i=1}^{n} \varphi_{i+n}(x) \phi_{i+n}(t), \end{aligned} \tag{C.19}$$

$$\begin{aligned} \dot{w}_{R,r}(x,t) &= \sum_{i=1}^{n} \varphi_i(x) \dot{q}_i(t), \;\; \dot{w}_{L,r}(x,t) = \sum_{i=1}^{n} \varphi_{i+n}(x) \dot{q}_{i+n}(t), \\ \dot{w}_{R,b}(x,t) &= \sum_{i=1}^{n} \varphi_i(x) \dot{\phi}_i(t), \;\; \dot{w}_{L,b}(x,t) = \sum_{i=1}^{n} \varphi_{i+n}(x) \dot{\phi}_{i+n}(t), \end{aligned} \tag{C.20}$$

$$\begin{aligned} w''_{R,r}(x,t) &= \sum_{i=1}^{n} \varphi''_i(x) q_i(t), \;\; w''_{L,r}(x,t) = \sum_{i=1}^{n} \varphi''_{i+n}(x) q_{i+n}(t), \\ w''_{R,b}(x,t) &= \sum_{i=1}^{n} \varphi''_i(x) \phi_i(t), \;\; w''_{L,b}(x,t) = \sum_{i=1}^{n} \varphi''_{i+n}(x) \phi_{i+n}(t), \end{aligned} \tag{C.21}$$

$$\varphi_i(x) = \sqrt{\frac{2}{L}} \sin\left(\frac{i\pi x}{L}\right), i = 1, 2, ..., n. \tag{C.22}$$

Here, the parameters q and ϕ represent the generalized coordinates for the displacement of the rail and bridge beam structure, respectively, and φ stands for the oscillation form produced with the beam's easily supported boundary conditions. The parameter n defines the simply supported beam's mode number.

The orthogonality conditions of mode shape the oscillations are shown in Eq. (C. 23), where δ_{ij} stands for Kronecker delta. Also, while the first subscript represents the right rail beam, the second represents the left rail beam [26].

$$\int_0^L \mu_{1,2} \varphi_{1,2\ i}(x) \varphi_{1,2\ j}(x) dx = N_{1,2\ i} \delta_{1,2\ ij}, \;\; \int_0^L (EI)_{1,2} \varphi''_{1,2\ i}(x) \varphi''_{1,2\ j}(x) dx = \Pi_{1,2\ i} \delta_{1,2\ ij} \tag{C.23}$$

The vertical motion of the rail or bridge, $w_{r,b}(x,t)$, denotes the displacement of any x point on the beam at any t time in relation to the train's entry point into the bridge. Only vertical dynamic behaviors are considered, and lateral displacements are neglected.

$$\frac{d}{dt}\left(\frac{\partial L}{\partial \dot{\lambda}_i(t)}\right) - \frac{\partial L}{\partial \lambda_i(t)} + \frac{\partial D}{\partial \dot{\lambda}_i(t)} = Q_i, \;\; i = 1, 2, ..., 32, \tag{C.24}$$

$$Q_i = \int_0^L \varphi_i(x) f_{ci}(x,t) dx, \;\; i = 1, 2, ..., 32, \tag{C.25}$$

The generalized coordinates of the track and beam are given as follows. This study considers the first four vibration modes of track parts, along with the rail and bridge beams.

$$\lambda(t) = \left\{ \begin{array}{c} q_1(t) q_2(t) q_3(t) q_4(t) q_5(t) q_6(t) q_7(t) q_8(t) \\ \gamma_1(t) \gamma_2(t) \gamma_3(t) \gamma_4(t) \gamma_5(t) \gamma_6(t) \gamma_7(t) \gamma_8(t) \\ \psi_1(t) \psi_2(t) \psi_3(t) \psi_4(t) \psi_5(t) \psi_6(t) \psi_7(t) \psi_8(t) \\ \phi_1(t) \phi_2(t) \phi_3(t) \phi_4(t) \phi_5(t) \phi_6(t) \phi_7(t) \phi_8(t) \end{array} \right\}^T, \begin{array}{l} q \rightarrow \text{ Rail beam} \\ \gamma \rightarrow \text{ Sleeper} \\ \psi \rightarrow \text{Ballast} \\ \phi \rightarrow \text{ Bridge beam} \end{array} \tag{C.26}$$

The motion equation of the track subsystem given in Fig. 1d is produced using the beam displacement specified in Eq. (C. 23), and the Galerkin's approach, together with the orthogonality constraints provided in Eq. (C. 21). The equations of motion for the right rail beam, right sleeper, right ballast and, right bridge beam are given below:

The motion equation of the right rail beam is given by Eq. (C. 27):

$$
\begin{aligned}
\ddot{q}_{i(t)} = & -S_{1,i}q_{i(t)}\,/N_{1,i} - c_1\dot{q}_{i(t)}\,/N_{1,i} \\
& +\varphi_i(\xi_{1R},t)\,/N_{1,i}\left[\begin{array}{l} c_{w1y}\left[\dot{r}_{b1y} - \sum_{i=1}^{n}\varphi_i(\xi_{1R},t)\dot{q}_i + \dot{\theta}_{b1z}l_{w1} - \dot{\theta}_{b1x}d + \dot{\theta}_{w1x}d\right] \\ +k_{w1y}\left[r_{b1y} - \sum_{i=1}^{n}\varphi_i(\xi_{1R},t)q_i + \theta_{b1z}l_{w1} - \theta_{b1x}d + \theta_{w1x}d\right] - f_{g1}\end{array}\right] \\
& +\varphi_i(\xi_{2R},t)\,/N_{1,i}\left[\begin{array}{l} c_{w2y}\left[\dot{r}_{b1y} - \sum_{i=1}^{n}\varphi_i(\xi_{2R},t)\dot{q}_i - \dot{\theta}_{b1z}l_{w2} - \dot{\theta}_{b1x}d + \dot{\theta}_{w2x}d\right] \\ +k_{w2y}\left[r_{b1y} - \sum_{i=1}^{n}\varphi_i(\xi_{2R},t)q_i - \theta_{b1z}l_{w2} - \theta_{b1x}d + \theta_{w2x}d\right] - f_{g2}\end{array}\right] \\
& +\varphi_i(\xi_{3R},t)\,/N_{1,i}\left[\begin{array}{l} c_{w3y}\left[\dot{r}_{b2y} - \sum_{i=1}^{n}\varphi_i(\xi_{3R},t)\dot{q}_i + \dot{\theta}_{b2z}l_{w3} - \dot{\theta}_{b2x}d + \dot{\theta}_{w3x}d\right] \\ +k_{w3y}\left[r_{b2y} - \sum_{i=1}^{n}\varphi_i(\xi_{3R},t)q_i + \theta_{b2z}l_{w3} - \theta_{b2x}d + \theta_{w3x}d\right] - f_{g3}\end{array}\right] \\
& +\varphi_i(\xi_{4R},t)\,/N_{1,i}\left[\begin{array}{l} c_{w4y}\left[\dot{r}_{b2y} - \sum_{i=1}^{n}\varphi_i(\xi_{4R},t)\dot{q}_i - \dot{\theta}_{b2z}l_{w4} - \dot{\theta}_{b2x}d + \dot{\theta}_{w4x}d\right] \\ +k_{w4y}\left[r_{b2y} - \sum_{i=1}^{n}\varphi_i(\xi_{4R},t)q_i - \theta_{b2z}l_{w4} - \theta_{b2x}d + \theta_{w4x}d\right] - f_{g4}\end{array}\right]
\end{aligned}
\tag{C.27}
$$

The symbol expressed as F_l in Eq. (C.27) and specified as Lorentz force was found in Eq. (5) and integrated into the differential equation of the bridge.

The motion of the equation of the right sleeper is obtained as follows:

$$
\ddot{w}_{s,r} = \frac{1}{m_s}\left[k_p\left[w_{r,r} - w_{s,r}\right] - k_b\left[w_{s,r} - w_{ba,r}\right] + c_p\left[\dot{w}_{r,r} - \dot{w}_{s,r}\right] - c_b\left[\dot{w}_{s,r} - \dot{w}_{ba,r}\right]\right] \tag{C.28}
$$

The motion of the equation of the right ballast is rewritten below:

$$
\ddot{w}_{ba,r} = \frac{1}{m_{ba}}\left[k_b\left[w_{s,r} - w_{ba,r}\right] - k_f\left[w_{ba,r} - w_{b,r}\right] + c_b\left[\dot{w}_{s,r} - \dot{w}_{ba,r}\right] - c_f\left[\dot{w}_{ba,r} - \dot{w}_{b,r}\right]\right] \tag{C.29}
$$

Following is a description of the right bridge beam's equation of motion.

$$
\begin{aligned}
\ddot{\phi}_{i(t)} = & -S_{b1,i}\phi_{i(t)}\,/N_{b1,\ i} - c_b\dot{\phi}_{i(t)}\,/N_{b1,i} + F_l\,/N_{1,i} - c_f\varphi_i(\xi_R,t)\,/N_{b1,i}\left[\dot{w}_{ba,R} - \sum_{i=1}^{n}\varphi_i(\xi_R,t)\dot{\phi}_i\right] \\
& -k_f\varphi_i(\xi_R,t)\,/N_{b1,i}\left[w_{ba,R} - \sum_{i=1}^{n}\varphi_i(\xi_R,t)\phi_i\right]
\end{aligned}
\tag{C.30}
$$

The right rail beam's second-order equation is provided in Eq. (C. 27). The f_g symbol, in this instance, depicts the train's static forces on the bridge beam.

References

[1] Zhai W, Han Z, Chen Z, Ling L, Zhu S. Train–track–bridge dynamic interaction: a state-of-the-art review. Veh Syst Dyn 2019;57:984–1027. https://doi.org/10.1080/00423114.2019.1605085.

[2] Frýba L. Vibration of solids and structures under moving loads. Thomas Telford House; 1999.

[3] Biggs JM. Introduction to structural dynamics. McGraw- Hill; 1964.

[4] Liu K, De Roeck G, Lombaert G. The effect of dynamic train-bridge interaction on the bridge response during a train passage. J Sound Vib 2009;325:240–51. https://doi.org/10.1016/j.jsv.2009.03.021.

[5] Fitzgerald PC, Malekjafarian A, Cantero D, OBrien EJ, Prendergast LJ. Drive-by scour monitoring of railway bridges using a wavelet-based approach. Eng Struct 2019;191:1–11. https://doi.org/10.1016/j.engstruct.2019.04.046.

[6] Zhou S, Song G, Wang R, Ren Z, Wen B. Nonlinear dynamic analysis for coupled vehicle-bridge vibration system on nonlinear foundation. Mech Syst Signal Process 2017;87:259–78. https://doi.org/10.1016/j.ymssp.2005.08.023.

[7] Yang YB, Wu YS. A versatile element for analyzing vehicle-bridge interaction response. Eng Struct 2001;23:452–69. https://doi.org/10.1016/S0141-0296(00)00065-1.

[8] Gandhi P, Adarsh S, Ramachandran KI. Performance analysis of half car suspension model with 4 DOF using PID, LQR, FUZZY and ANFIS controllers. Procedia Comput Sci 2017;115:2–13. https://doi.org/10.1016/j.procs.2017.09.070.

[9] Li Q, Deng Z, Wang L, Li H, Zhang J, Rodriguez EF. Active vibration control of secondary suspension based on high-temperature superconducting maglev vehicle system. Phys C Supercond Appl 2021;585. https://doi.org/10.1016/j.physc.2021.1353872.

[10] Yang JP, Sun JY. Pitching effect of a three-mass vehicle model for analyzing vehicle-bridge interaction. Eng Struct 2020;224:111248. https://doi.org/10.1016/j.engstruct.2020.111248.

[11] Guo W, Zeng C, Gou H, Gu Q, Wang T, Zhou H, et al. Real-time hybrid simulation of high-speed train-track-bridge interactions using the moving load convolution integral method. Eng Struct 2021;228:111537. https://doi.org/10.1016/j.engstruct.2020.111537.

[12] El Kacimi A, Woodward PK, Laghrouche O, Medero G. Time domain 3D finite element modelling of train-induced vibration at high speed. Comput Struct 2013;118:66–73. https://doi.org/10.1016/j.compstruc.2012.07.011.

[13] Wu B, Zeng Y, Zhou Z, Wu G, Lu H. Vibration prediction based on the coupling method of half-train model and 3D refined finite element ground model. Comput Geotech 2021;134:104133. https://doi.org/10.1016/j.compgeo.2021.104133.

[14] Koç MA. Finite element and numerical vibration analysis of a Timoshenko and Euler-Bernoulli beams traversed by a moving high-speed train. J Braz Soc Mech Sci Eng 2021;7. https://doi.org/10.1007/s40430-021-02835-7.

[15] Chen Z, Fang H. An alternative solution of train-track dynamic interaction. Shock Vib 2019;2019. https://doi.org/10.1155/2019/1859261.

[16] Dai J, Han M, Ang KK. Moving element analysis of partially filled freight trains subject to abrupt braking. Int J Mech Sci 2019;151:85–94. https://doi.org/10.1016/j.ijmecsci.2018.11.011.

[17] Stojanović V, Petković MD, Deng J. Stability of vibrations of a moving railway vehicle along an infinite complex three-part viscoelastic beam/foundation system. Int J Mech Sci 2018;136:155–68. https://doi.org/10.1016/j.ijmecsci.2017.12.024.

[18] Jiang L, Liu X, Xiang P, Zhou W. Train-bridge system dynamics analysis with uncertain parameters based on new point estimate method. Eng Struct 2019;199:109454. https://doi.org/10.1016/j.engstruct.2019.109454.

[19] Olmos JM, Astiz MA. Analysis of the dynamic response of high pier viaducts under high-speed train travel. In: Proceedings of the 8th international conference structure dynamic EURODYN. 56; 2011. p. 1438–45.

[20] Yang CJ, Xu Y, Zhu WD, Fan W, Zhang WH, Mei GM. A three-dimensional modal theory-based Timoshenko finite length beam model for train-track dynamic analysis. J Sound Vib 2020;479:1–22. https://doi.org/10.1016/j.jsv.2020.115363.

[21] Shamsi M, Ghanbari A. Nonlinear dynamic analysis of Qom Monorail Bridge considering soil-pile-bridge-train Interaction. Transp Geotech 2020;22:100309. https://doi.org/10.1016/j.trgeo.2019.100309.

[22] Wang M, Li XZ, Xiao J, Zou QY, Sha HQ. An experimental analysis of the aerodynamic characteristics of a high-speed train on a bridge under crosswinds. J Wind Eng Ind Aerodyn 2018;177:92–100. https://doi.org/10.1016/j.jweia.2018.03.021.

[23] Stoura CD, Dimitrakopoulos EG. Additional damping effect on bridges because of vehicle-bridge interaction. J Sound Vib 2020;476:1–16. https://doi.org/10.1016/j.jsv.2020.115294.

[24] Yau JD, Martínez-Rodrigo MD, Doménech A. An equivalent additional damping approach to assess vehicle-bridge interaction for train-induced vibration of short-span railway bridges. Eng Struct 2019;188:469–79. https://doi.org/10.1016/j.engstruct.2019.01.144.

[25] Zhang N, Tian Y, Xia H. A train-bridge dynamic interaction analysis method and its experimental validation. Engineering 2016;2:528–36. https://doi.org/10.1016/J.ENG.2016.04.012.

[26] Koç MA, Esen İ, Eroğlu M, Çay Y. A new numerical method for analysing the interaction of a bridge structure and travelling cars due to multiple high-speed trains. Int J Heavy Veh Syst 2021;28.

[27] Grossoni I, Powrie W, Zervos A, Bezin Y, Le L. Transportation Geotechnics Modelling railway ballasted track settlement in vehicle-track interaction analysis. Transp Geotech 2021;26:100433. https://doi.org/10.1016/j.trgeo.2020.100433.

[28] Xu YL, Li Q, Wu DJ, Chen ZW. Stress and acceleration analysis of coupled vehicle and long-span bridge systems using the mode superposition method. Eng Struct 2010;32:1356–68. https://doi.org/10.1016/j.engstruct.2010.01.013.

[29] Yang SC, Hwang SH. Train-track-bridge interaction by coupling direct stiffness method and mode superposition method. J Bridg Eng 2016;21. https://doi.org/10.1061/(asce)be.1943-5592.0000852. 04016058.

[30] Zhu Z, Gong W, Wang L, Li Q, Bai Y, Yu Z, et al. An efficient multi-time-step method for train-track-bridge interaction. Comput Struct 2018;196:36–48. https://doi.org/10.1016/j.compstruc.2017.11.004.

[31] Melo LRT, Malveiro J, Ribeiro D, Calçada R, Bittencourt T. Dynamic analysis of the train-bridge system considering the non-linear behaviour of the track-deck interface. Eng Struct 2020;220:110980. https://doi.org/10.1016/j.engstruct.2020.110980.

[32] Hirzinger B, Adam C, Salcher P. Dynamic response of a non-classically damped beam with general boundary conditions subjected to a moving mass-spring-damper system. Int J Mech Sci 2020;185. https://doi.org/10.1016/j.ijmecsci.2020.105877.

[33] Tahiri M, Khamlichi A, Bezzazi M. Nonlinear analysis of the ballast influence on the train-bridge resonance of a simply supported railway bridge. Structures 2022;35:303–13. https://doi.org/10.1016/j.istruc.2021.11.020.

[34] König P, Salcher P, Adam C, Hirzinger B. Dynamic analysis of railway bridges exposed to high-speed trains considering the vehicle–track–bridge–soil interaction. Acta Mech 2021. https://doi.org/10.1007/s00707-021-03079-1.

[35] Zhen B, Xu J, Sun J. Analytical solutions for steady state responses of an infinite Euler-Bernoulli beam on a nonlinear viscoelastic foundation subjected to a harmonic moving load. J Sound Vib 2020;476. https://doi.org/10.1016/j.jsv.2020.115271.

[36] Esen I. International Journal of Mechanical Sciences Dynamic response of a functionally graded Timoshenko beam on two-parameter elastic foundations due to a variable velocity moving mass. Int J Mech Sci 2019;153–154:21–35. https://doi.org/10.1016/j.ijmecsci.2019.01.033.

[37] Esen I. Dynamic response of functional graded Timoshenko beams in a thermal environment subjected to an accelerating load. Eur J Mech A Solids 2019;78:103841. https://doi.org/10.1016/j.euromechsol.2019.103841.

[38] Pala Y, Beycimen S, Kahya C. Damped vibration analysis of cracked Timoshenko beams with restrained end conditions. J Braz Soc Mech Sci Eng 2020;42:1–16. https://doi.org/10.1007/s40430-020-02558-1.

[39] Zhang X, Thompson D, Sheng X. Differences between Euler-Bernoulli and Timoshenko beam formulations for calculating the effects of moving loads on a periodically supported beam. J Sound Vib 2020;481:115432. https://doi.org/10.1016/j.jsv.2020.115432.

[40] Hoang T, Duhamel D, Foret G. Dynamical response of a Timoshenko beams on periodical nonlinear supports subjected to moving forces. Eng Struct 2018;176:673–80. https://doi.org/10.1016/j.engstruct.2018.09.028.

[41] Wang L, Zhu Z, Bai Y, Li Q, Costa PA, Yu Z. A fast random method for three-dimensional analysis of train-track-soil dynamic interaction. Soil Dyn Earthq Eng 2018;115:252–62. https://doi.org/10.1016/j.soildyn.2018.08.021.

[42] Mizrak C, Esen I. Determining effects of wagon mass and vehicle velocity on vertical vibrations of a rail vehicle moving with a constant acceleration on a bridge using experimental and numerical methods. Shock Vib 2015;2015. https://doi.org/10.1155/2015/183450.

[43] Liu X, Jiang L, Lai Z, Xiang P, Chen Y. Sensitivity and dynamic analysis of train-bridge coupled system with multiple random factors. Eng Struct 2020;221:111083. https://doi.org/10.1016/j.engstruct.2020.111083.

[44] Stoura CD, Paraskevopoulos E, Dimitrakopoulos EG, Natsiavas S. A dynamic partitioning method to solve the vehicle-bridge interaction problem. Comput Struct 2021;251:106547. https://doi.org/10.1016/j.compstruc.2021.106547.

[45] Lou P, Au FTK. Finite element formulae for internal forces of Bernoulli-Euler beams under moving vehicles. J Sound Vib 2013;332:1533–52. https://doi.org/10.1016/j.jsv.2012.11.011.

[46] Olmos JM, Astiz M. Improvement of the lateral dynamic response of a high pier viaduct under turbulent wind during the high-speed train travel. Eng Struct 2018;165:368–85. https://doi.org/10.1016/j.engstruct.2018.03.054.

[47] Xu L, Zhai W. A three-dimensional dynamic model for train-track interactions. Appl Math Model 2019;76:443–65. https://doi.org/10.1016/j.apm.2019.04.037.

[48] Van Do VN, Ong TH, Thai CH. Dynamic responses of Euler–Bernoulli beam subjected to moving vehicles using isogeometric approach. Appl Math Model 2017;51:405–28. https://doi.org/10.1016/j.apm.2017.06.037.

[49] Xu L, Zhai W. A three-dimensional model for train-track-bridge dynamic interactions with hypothesis of wheel-rail rigid contact. Mech Syst Signal Process 2019;132:471–89. https://doi.org/10.1016/j.ymssp.2019.04.025.

[50] He Q, Cai C, Zhu S, Wang K, Zhai W. An improved dynamic model of suspended monorail train-bridge system considering a tyre model with patch contact. Mech Syst Signal Process 2020;144:106865. https://doi.org/10.1016/j.ymssp.2020.106865.

[51] Van Vinh P, Van Chinh N, Tounsi A. Static bending and buckling analysis of bi-directional functionally graded porous plates using an improved first-order shear deformation theory and FEM. Eur J Mech A Solids 2022;96:104743. https://doi.org/10.1016/j.euromechsol.2022.104743.

[52] Zhang J, Gao Q, Tan SJ, Zhong WX. A precise integration method for solving coupled vehicle-track dynamics with nonlinear wheel-rail contact. J Sound Vib 2012;331:4763–73. https://doi.org/10.1016/j.jsv.2012.05.033.

[53] Li Q, Xu YL, Wu DJ. Concrete bridge-borne low-frequency noise simulation based on traintrackbridge dynamic interaction. J Sound Vib 2012;331:2457–70. https://doi.org/10.1016/j.jsv.2011.12.031.

[54] Ouyang H. Moving-load dynamic problems: a tutorial (with a brief overview). Mech Syst Signal Process 2011;25:2039–60. https://doi.org/10.1016/j.ymssp.2010.12.010.

[55] Zhai W. Vehicle–track coupled dynamics models. Veh Track Coupled Dyn 2020. https://doi.org/10.1007/978-981-32-9283-3_42.

[56] Al-Furjan MSH, Habibi M, Ghabussi A, Safarpour H, Safarpour M, Tounsi A. Non-polynomial framework for stress and strain response of the FG-GPLRC disk using three-dimensional refined higher-order theory. Eng Struct 2021;228:111496. https://doi.org/10.1016/j.engstruct.2020.111496.

[57] Kong F, Dong F, Duan M, Habibi M, Safarpour H, Tounsi A. On the vibrations of the Electrorheological sandwich disk with composite face sheets considering pre and post-yield regions. Thin Walled Struct 2022;179:109631. https://doi.org/10.1016/j.tws.2022.109631.

[58] Al-Furjan MSH, Habibi M, Ni J, won JD, Tounsi A. Frequency simulation of viscoelastic multi-phase reinforced fully symmetric systems. Eng Comput 2020. https://doi.org/10.1007/s00366-020-01200-x.

[59] Hasrati E, Ansari R, Rouhi H. Nonlinear free vibration analysis of shell-type structures by the variational differential quadrature method in the context of six-parameter shell theory. Int J Mech Sci 2019;151:33–45. https://doi.org/10.1016/j.ijmecsci.2018.10.053.

[60] Shen J, Wang H, Zheng S. Size-dependent pull-in analysis of a composite laminated micro-beam actuated by electrostatic and piezoelectric forces: Generalized differential quadrature method. Int J Mech Sci 2018;135:353–61. https://doi.org/10.1016/j.ijmecsci.2017.11.002.

[61] Garg A, Belarbi MO, Tounsi A, Li L, Singh A, Mukhopadhyay T. Predicting elemental stiffness matrix of FG nanoplates using Gaussian Process Regression based surrogate model in framework of layerwise model. Eng Anal Bound Elem 2022;143:779–95. https://doi.org/10.1016/j.enganabound.2022.08.001.

[62] Huang X, Hao H, Oslub K, Habibi M, Tounsi A. Dynamic stability/instability simulation of the rotary size-dependent functionally graded microsystem. Eng Comput 2021. https://doi.org/10.1007/s00366-021-01399-3.

[63] Kumar Y, Gupta A, Tounsi A. Size-dependent vibration response of porous graded nanostructure with FEM and nonlocal continuum model. Adv Nano Res 2021;11:1–17. https://doi.org/10.12989/anr.2021.11.1.001.

[64] Lee JW, Lee JY. Free vibration analysis of functionally graded Bernoulli-Euler beams using an exact transfer matrix expression. Int J Mech Sci 2017;122:1–17. https://doi.org/10.1016/j.ijmecsci.2017.01.011.

[65] Jalaei MH, Arani AG, Nguyen-Xuan H. Investigation of thermal and magnetic field effects on the dynamic instability of FG Timoshenko nanobeam employing nonlocal strain gradient theory. Int J Mech Sci 2019;161-162:105043. https://doi.org/10.1016/j.ijmecsci.2019.105043.

[66] Arani AG, Jalaei MH. Investigation of the longitudinal magnetic field effect on dynamic response of viscoelastic graphene sheet based on sinusoidal shear deformation theory. Phys B Condens Matter 2017;506:94–104. https://doi.org/10.1016/j.physb.2016.11.004.

[67] Esen I, Özarpa C, Eltaher MA. Free vibration of a cracked FG microbeam embedded in an elastic matrix and exposed to magnetic field in a thermal environment.

Compos Struct 2021;261:113552. https://doi.org/10.1016/j.compstruct.2021.113552.
[68] Esen I, Abdelrhmaan AA, Eltaher MA. Free vibration and buckling stability of FG nanobeams exposed to magnetic and thermal fields. Eng Comput 2021. https://doi.org/10.1007/s00366-021-01389-5.
[69] Esen I. Response of a micro-capillary system exposed to a moving mass in magnetic field using nonlocal strain gradient theory. Int J Mech Sci 2020;188:105937. https://doi.org/10.1016/j.ijmecsci.2020.105937.
[70] Bai Y, Suhatril M, Cao Y, Forooghi A, Assilzadeh H. Hygro–thermo–magnetically induced vibration of nanobeams with simultaneous axial and spinning motions based on nonlocal strain gradient theory. Eng Comput 2021. https://doi.org/10.1007/s00366-020-01218-1.
[71] Ebrahimi F, Dabbagh A. Magnetic field effects on thermally affected propagation of acoustical waves in rotary double-nanobeam systems. Waves Random Complex Media 2021;31:25–45. https://doi.org/10.1080/17455030.2018.1558308.
[72] Sobhy M, Abazid MA. Dynamic and instability analyses of FG graphene-reinforced sandwich deep curved nanobeams with viscoelastic core under magnetic field effect. Compos Part B Eng 2019;174:106966. https://doi.org/10.1016/j.compositesb.2019.106966.
[73] Kraus J.D. Electromagnetismo. DF Mc Graw Hjlf 1986.
[74] Özmen R, Kılıç R, Esen I. Thermomechanical vibration and buckling response of nonlocal strain gradient porous FG nanobeams subjected to magnetic and thermal fields. Mech Adv Mater Struct 2022;0:1–20. https://doi.org/10.1080/15376494.2022.2124000.
[75] Museros P. Vehicle-bridge interaction and resonance effects in simply supported bridges for high speed lines. Tech Univ Madrid; 2002. https://doi.org/10.1016/S0022-460X(02)01463-3.
[76] Frýba L. A rough assessment of railway bridges for high speed trains. Eng Struct 2001;23:548–56. https://doi.org/10.1016/S0141-0296(00)00057-2.
[77] Museros P, Alarcón E. Influence of the second bending mode on the response of high-speed bridges at resonance. J Struct Eng 2005;131:405–15. https://doi.org/10.1061/(ASCE)0733-9445(2005)131:3(405).
[78] Yau JD, Yang YB. Vertical accelerations of simple beams due to successive loads traveling at resonant speeds. J Sound Vib 2006;289:210–28. https://doi.org/10.1016/j.jsv.2005.02.037.
[79] Youcef K, Sabiha T, El Mostafa D, Ali D, Bachir M. Dynamic analysis of train-bridge system and riding comfort of trains with rail irregularities. J Mech Sci Technol 2013;27:951–62. https://doi.org/10.1007/s12206-013-0206-8.
[80] Garg VK, Dukkipati RV. Dynamics of railway vehicle systems. Acad Press Canada 1984;14:245–7. https://doi.org/10.1016/0378-3804(87)90070-2.
[81] Gao Y. Field analytical investigation of a 3D dynamic train-track interaction model at critical speeds 2016.
[82] Yau JD, Frýba L. Response of suspended beams due to moving loads and vertical seismic ground excitations. Eng Struct 2007;29:3255–62. https://doi.org/10.1016/j.engstruct.2007.10.001.